

The linear-time-invariance notion of the Koopman analysis. Part 2. Dynamic Koopman modes, physics interpretations and phenomenological analysis of the prism wake

Cruz Y. Li^{1,2}, Zengshun Chen¹, Tim K.T. Tse^{2,†},
Asiri Umenga Weerasuriya², Xuelin Zhang³, Yunfei Fu² and Xisheng Lin²

¹Department of Civil Engineering, Chongqing University, Chongqing, PR China

²Department of Civil and Environmental Engineering, The Hong Kong University of Science and Technology, Hong Kong SAR, PR China

³School of Atmospheric Sciences, Sun Yat-sen University, Zhuhai, PR China

(Received 17 February 2022; revised 13 November 2022; accepted 8 January 2023)

This serial work presents a linear-time-invariance (LTI) notion to the Koopman analysis, finding consistent and physically meaningful Koopman modes and addressing a long-standing problem of fluid mechanics: deterministically relating the fluid excitations and corresponding structure reactions. Part 1 (Li *et al.*, *Phys. Fluids*, vol. 34, no. 12, p. 125136) developed the Koopman-LTI architecture and applied it to a pedagogical prism wake. By a systematic analytical procedure, the Koopman-LTI generated sampling-independent linear models that captured all the recurring dynamics embedded in the input data, finding six corresponding, orthogonal, and in-synch fluid–structure mechanisms. This Part 2 analyses the six modal duplets to underpin their physical implications, providing a phenomenological analysis of the subcritical prism wake. Visualizing the newly proposed dynamic Koopman modes, results show that two mechanisms at $St_1 = 0.1242$ and $St_5 = 0.0497$ describe shear layer dynamics, the associated Bérnard–Kármán shedding and turbulence production, which together overwhelm the upstream and crosswind walls by instigating a reattachment-type of reaction. The on-wind walls' dynamical similarity renders them a spectrally unified fluid–structure interface. Another four harmonic counterparts, namely the subharmonic at $St_7 = 0.0683$, the second harmonic at $St_3 = 0.2422$, and two ultra-harmonics at $St_7 = 0.1739$ and $St_{13} = 0.1935$, govern the downstream wall. Finally, this work discovered the vortex breathing phenomenon, describing the constant energy exchange in the wake's circulation-entrainment-deposition processes. With the Koopman-LTI, one may pinpoint the exact excitations responsible for a specific structure reaction, benefiting future investigations into fluid–structure interactions and nonlinear, stochastic systems.

† Email address for correspondence: timkttse@ust.hk

Key words: flow-structure interactions, wakes, low-dimensional models

1. Introduction

The omnipresence of fluid–structure systems calls for persistent research and exploration into their fluid mechanics. To date, fluids’ volatility, their nonlinear interactive mechanisms with structures and the unsolved Navier–Stokes equations leave this topic a persisting enigma. Fortunately, recent advancements in data science have offered a brand-new pathway to the solution (Budišić, Mohr & Mezić 2012; Kutz *et al.* 2016; Lusch, Kutz & Brunton 2018; Raissi *et al.* 2019). Seven decades after the ingenious Koopman theory (Koopman 1931; Koopman & Neumann 1932), its mathematical promise was brought to life by the pioneers of data science (Mezić 2005; Rowley *et al.* 2009; Schmid 2010; Mauroy & Mezić 2012). Since then, the Koopman analysis has been pervasively applied to fluid problems with success, with many of them directly involving fluid–structure interactive or reactive systems (Muld, Efrainsson & Henningson 2012; Carlsson *et al.* 2014; Magionesi *et al.* 2018; Garicano-Mena *et al.* 2019; Miyawala & Jaiman 2019; Page & Kerswell 2019; Eivazi *et al.* 2020; Li, Tse & Hu 2020*a,b*; Wu, Meneveau & Mittal 2020; Dotto *et al.* 2021; Herrmann *et al.* 2021; Jang *et al.* 2021; Li *et al.* 2021; 2022*c,d,e*; Liu *et al.* 2021*a,b,c*; Chen *et al.* 2022; Li, Chen, & Tse 2022*b*). Several works have summarized the current status of the Koopman analysis in fluid applications and subordinate data-driven algorithms (Mezić 2013; Rowley & Dawson 2017; Taira *et al.* 2017; Schmid 2022; Li *et al.* 2023).

On a celebratory note, we observed that most organized research on the Koopman theory was led by applied mathematicians and focused on algorithmic development (Schmid *et al.* 2011; Budišić *et al.* 2012; Brunton *et al.* 2016). Analysing the algorithmic output is often left to individual, case-by-case interpretations. The present serial effort aims to highlight Koopmanism’s unique potentials for analysing fluid–structure systems—deterministically relating observed structure reactions to their flow excitation origins. In Part 1 (Li *et al.* 2022*a*), we proposed the linear-time-invariance (LTI) notion and developed an organized and replicable analytical framework called the Koopman-LTI architecture (see figure 1). With a pedagogical demonstration on the subcritical prism wake (i.e. a rigid, infinitely long prism reacting to fluid excitations) and similarity-matrix dynamic mode decomposition (DMD) algorithm as the Koopman approximator, Part 1 successfully:

- (1) generated a sampling independent Koopman linearization that captured all the prominent recurring dynamics. The mean reconstruction error, root-mean-square (r.m.s.) reconstruction error and DMD approximation error of the Koopman modes were all at numerical zeros, O^{-12} , O^{-9} and O^{-8} , respectively;
- (2) disclosed w ’s trivial role in the convection-dominated free-shear flow, Reynolds stresses’ spectral description of cascading eddies, vortices’ sensitivity to dilation and indifference to distortion, and structure reactions’ origin in vortex activities;
- (3) reduced the subcritical wake during shear layer transition II into only six dominant excitation-reaction dynamics. The upstream and crosswind walls constitute a dynamically unified interface, which is dominated by only two mechanisms at $St = 0.1242$ and $St = 0.0497$ (Class 1). The downstream wall remains a distinct interface and is dominated by four other mechanisms at $St = 0.1739$, $St = 0.0683$, $St = 0.1925$ and $St = 0.2422$ (Class 2).

The linear-time-invariance notion of the Koopman analysis

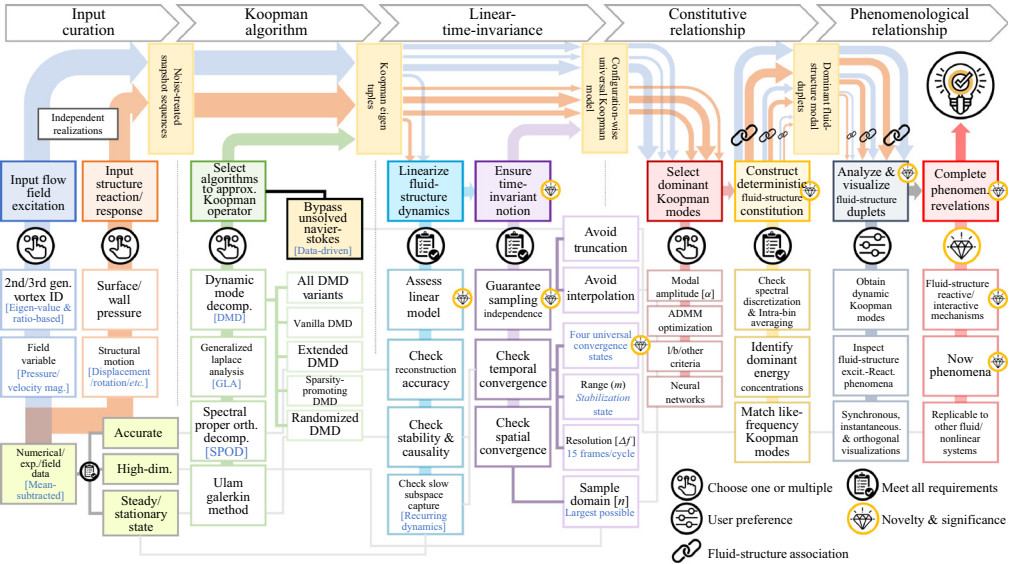


Figure 1. Koopman linear-time-invariance (Koopman-LTI) architecture. It consists of the input curation, Koopman algorithm, linear-time-invariance, constitutive relationship and phenomenological relationship modules. Each module contains several submodules with requirements or options. The Koopman-LTI is purely data-driven, theoretically accommodating all input types and solution algorithms that can accurately approximate the Koopman eigen tuples.

By completing the input curation, Koopman algorithm, linear-time-invariance and constitutive relationship modules, the fluid–structure constitution has been established. The complete analysis essentially comes down to understanding the six mechanisms, which this Part 2 will address through the final phenomenological relationship module.

Phenomenology, the study of phenomena, is the essential path to solution for many fluid–structure systems. As Roshko (1993) remarked:

‘The problem of bluff body flow remains almost entirely in the empirical, descriptive realm of knowledge.’

In this paper, we propose a methodical improvement, the dynamic Koopman mode, to visualize in-synch, instantaneously varying flow field coherent structures (Hussain 1986) and the corresponding structure reactions, overcoming the phase issues that often trouble static visualizations of the Koopman modes. The newly proposed dynamic Koopman modes also give phenomenological consolidation to spectral fluid–structure constitutions, disclosing the underlying mechanisms and enabling normalizable notions for inter-modal comparisons. In composition, following the introduction here, § 2 analyses the Class 1 mechanisms, § 3 focuses on the Class 2 mechanisms, § 4 presents a newly discovered vortex breathing phenomenon and § 5 offers a summary of the major findings.

2. A brief recapitulation

We briefly present some essential nomenclature and information inherited from Part 1 to facilitate better readability. Figure 1 presents the overall Koopman-LTI architecture, in which this Part 2 focuses exclusively on the final phenomenological relationship section. Table 1 summarizes the ten most dominant eigen tuples for each measurable (highlighted), resulting in precisely 30 across the entire inventory. In total, 18 field and wall measurables have been sampled as independent realizations (see table 2). Readers may find the relevant definitions in Li *et al.* (2022c). The subsequent text refers to the upstream (AB), top

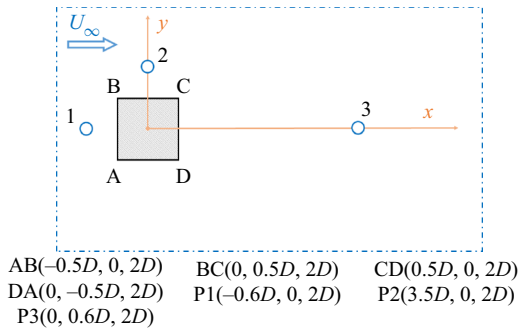


Figure 2. Orientation and location of the prism walls.

(BC), downstream (CD) and bottom (DA) walls according to the orientation in figure 2. After Liu (2019), this work also refers to the vorticity-based vortex identification criterion, namely $|\omega|$, as the first-generation vortex field, the eigenvalue-based criteria, namely q and λ_2 , as the second-generation, and the ratio-based criteria, namely Ω and $\tilde{\Omega}_R$, as the third-generation.

3. Phenomenological relationship (module 5) – Class 1

Before we begin, a limitation of modal visualization is clarified. Like any type of eigen mode shape, a dynamic Koopman mode only illustrates the bin-wise-averaged relationship of its spatiotemporal content, so the fluid–structure correspondence and synchrony are governed by the resolution of spectral discretization, highlighting the criticality of the LTI convergence. For this reason, we limit our discussion to the descriptive, phenomenological realm of fluid mechanics. Even so, as the upcoming sections will demonstrate, the physics embedded in the dynamic modes are already immensely rich. Readers are also reminded that mode shapes only describe the relative relationships between coherent dynamics, meaning the information contained in a mode is quintessentially identical to its opposite-sign counterpart. Therefore, in the subsequent sections, all terms of ‘positive’ and ‘negative’ refer to relative correlations instead of mathematical constitution. According to Lander *et al.* (2016), we also define the prism base as the streamwise distance between the downstream wall and $2.5D$ and the near-wake as the after-wake up to $7D$. The ensuing discussions are also based on the dynamic Koopman modes, so each static mode shape image is supplemented by a movie file. Please refer to the supplementary material, available at <https://doi.org/10.1017/jfm.2023.36>, for the reduced-size and full HD files.

3.1. M_1 – shear layer dynamics and Bérnard–Kármán shedding

3.1.1. Pressure field P

We begin with the Class 1 mechanisms. Figure 3 presents the normalized dynamic Koopman mode M_1 ($St_1 = 0.1242$) of P inside the flow domain and on the walls of the prism. The multimedia file depicts the alternating occurrence, development and shrinkage of separation bubbles adhering to the crosswind walls, as well as the subsequent shedding of coherent wake structures. By frequency-matching, we visualize the in-synch behaviours of the flow field and the corresponding structure reactions.

Specifically, the upstream wall (AB) exhibits consistent morphology throughout the shedding cycle. Only near edges A and B, two slivers of extreme pressure alternate in sign. This is the familiar impression of stagnation and forced separation, as AB of

The linear-time-invariance notion of the Koopman analysis

Mode – frequency	Input data																
	Primary measurable					Turbulence					Vortex identification criteria						
	Wall (P)		Flow field			Reynolds stress			TKE	1st Gen.	2nd Gen.	3rd Gen.					
BC	DA	AB	CD	P	u	v	w	$ U $	$(u'v')$	$(u'w')$	$(v'w')$	(k)	$ \omega $	q	λ_2	Ω	$\tilde{\Omega}_R$
$M_1 - Sr_1 = 0.1242$	1	1	1	1	1	1	26	1	11	20	19	1	1	1	1	1	1
$M_2 - Sr_2 = 0.1180$	2	2	2	3	2	2	11	2	14	19	20	3	2	4	4	3	3
$M_3 - Sr_3 = 0.2422$	14	13	19	9	5	3	5	42	4	40	41	10	4	2	2	2	2
$M_4 - Sr_4 = 0.1304$	3	3	3	11	3	4	3	31	5	23	21	5	8	6	7	5	7
$M_5 - Sr_5 = 0.0497$	4	4	4	14	4	5	8	1	3	5	8	2	3	5	5	7	5
$M_6 - Sr_6 = 0.0745$	10	17	15	4	8	6	13	4	6	13	12	19	5	15	16	14	10
$M_7 - Sr_7 = 0.0683$	11	21	17	6	10	7	12	14	8	10	11	31	7	8	8	11	9
$M_8 - Sr_8 = 0.1428$	5	6	5	8	6	8	4	6	7	27	23	22	4	9	17	18	8
$M_9 - Sr_9 = 0.1739$	17	11	21	2	9	9	11	24	11	25	28	27	7	6	3	10	8
$M_{10} - Sr_{10} = 0.1118$	6	5	6	10	7	10	6	25	10	21	18	6	16	20	22	13	18
$M_{11} - Sr_{11} = 0.1366$	7	8	7	18	11	11	7	21	9	24	22	21	23	15	25	15	19
$M_{12} - Sr_{12} = 0.1056$	8	7	8	38	12	13	10	22	13	20	17	17	27	17	31	30	24
$M_{13} - Sr_{13} = 0.1925$	23	27	29	5	13	15	9	28	15	22	31	11	11	7	6	6	6
$M_{14} - Sr_{14} = 0.1553$	9	16	9	24	16	16	20	17	21	26	25	26	21	18	10	11	29
$M_{15} - Sr_{15} = 0.0559$	20	9	10	12	15	19	28	23	16	9	9	9	17	10	26	25	21
$M_{16} - Sr_{16} = 0.3664$	37	33	46	7	25	34	15	64	27	45	59	60	16	39	29	26	23
$M_{17} - Sr_{17} = 0.0994$	24	10	13	29	17	14	21	18	17	18	16	16	12	20	37	37	21
$M_{18} - Sr_{18} = 0.0373$	13	44	20	25	24	20	24	2	14	7	6	6	9	19	34	34	26
$M_{19} - Sr_{19} = 0.0311$	25	30	30	19	29	21	32	3	19	6	5	5	14	13	36	36	40
$M_{20} - Sr_{20} = 0.1677$	26	32	32	21	33	25	22	5	32	28	27	28	32	27	60	58	34
$M_{21} - Sr_{21} = 0.0807$	16	12	11	30	14	12	16	7	12	15	13	13	8	12	16	15	14
$M_{22} - Sr_{22} = 0.0248$	35	20	26	27	30	26	42	8	23	4	4	4	22	21	48	48	41
$M_{23} - Sr_{23} = 0.0124$	33	42	34	43	42	32	41	9	31	2	2	2	26	29	58	63	37
$M_{24} - Sr_{24} = 0.0435$	28	19	27	41	26	17	27	10	20	8	7	7	20	14	23	24	18
$M_{25} - Sr_{25} = 0.0062$	45	39	36	53	43	29	30	12	29	1	1	1	28	37	63	64	38
$M_{26} - Sr_{26} = 0.0186$	34	24	25	36	35	31	34	13	28	3	3	3	25	28	49	52	36
$M_{27} - Sr_{27} = 0.0621$	12	38	16	22	19	22	26	20	22	12	10	10	13	22	30	29	31
$M_{28} - Sr_{28} = 0.4161$	50	40	55	45	52	53	56	67	52	62	66	68	53	43	9	9	54
$M_{29} - Sr_{29} = 0.2236$	27	22	23	15	23	30	14	36	33	37	36	37	34	31	12	10	9
$M_{30} - Sr_{30} = 0.2484$	32	35	37	26	22	27	25	40	25	29	39	39	18	32	22	21	4

Table 1. Summary of 30 dominant modes and their respective $|\tilde{\alpha}_j|$ ranking in each Koopman-LTI system (highlighted: 10 most dominant).

Wall pressure	Flow field	Turbulence field	Vortex field
BC [Top wall]	P [Total pressure]	$\langle u'v' \rangle$ [Reynolds stress from u' and v']	$ \omega $ [Vorticity magnitude] Helmholtz (1858)
DA [Bottom wall]	u [x -velocity]	$\langle u'w' \rangle$ [Reynolds stress from u' and w']	Q [q -criterion] Hunt, Wray & Moin (1988)
AB [Upstream wall]	v [y -velocity]	$\langle u'w' \rangle$ [Reynolds stress from v' and w']	λ_2 [λ_2 -criterion] Jeong & Hussain (1995)
CD [Downstream wall]	w [z -velocity]	$\langle k \rangle$ [Turbulence kinetic energy]	Ω [Ω -criterion] Liu <i>et al.</i> (2016)
	$ U $ [Velocity magnitude]		$\tilde{\Omega}_R$ [$\tilde{\Omega}$ -Liutex criterion] Liu <i>et al.</i> (2018)

Table 2. Summary of the inventory consisting of 18 measurables.

all other Koopman modes show monotonous morphologies with the only difference in the frequency of the sign switch, meeting anticipations and explaining why the upstream wall contains the most stationary dynamics and has the highest growth/decay rate compared to its peers (figure 8 from Part 1).

However, the other three walls' reactions are dissimilar. The sign-alternating separation bubbles dictate the crosswind reactions. Take the top wall (BC) as an example (see figure 3a). When the bubble is emerging, an intense pressure band forms near the rear edge C (in blue), which is of opposite sign to the upstream (in red). As the bubble forms and grows, the band becomes increasingly weaker. At the maximum bubble intensity, the band becomes like-sign with the upstream and even the high-pressure portions (see figure 3b). Furthermore, the downstream wall (CD) is anti-symmetrically alternating, which is in evident congruence with the bisected architecture of the near-wake. Again, the downstream wall traces back to the behaviours of the separation bubbles, or more, the root in shear layer dynamics.

3.1.2. Velocity magnitude $|U|$

The velocity field is the most common realization of the flow field and may draw more morphological familiarity to the readers. Figure 4 presents the normalized dynamic Koopman mode M_1 ($St_1 = 0.1242$) of $|U|$ inside the flow domain and on the walls of the prism. The figure delineates two shear layers stemming off from the leading edges due to forced separation. Their in-synch motion with P confirms the fact that separation bubbles result from the closure circulation zones, which are directly turbulent without a laminar transition (Kiya & Sasaki 1983; Wu *et al.* 2020). M_1 also illustrates the shear layers' dispersion from initially intense wall jets into waning streams as they convect downstream, accompanied by continuous fluid entrainment and vorticity dilution. The shear layers also gain curvature in the process, drawing wake structures increasingly close to the afterbody and toward the downstream wall (figure 3b). The ultimate outcome is the impingement of the leading vortex (Unal & Rockwell 1988a,b), also known as reattachment.

The aforementioned wall reactions link directly to the shear layers. Taking the top wall (BC) as an example again, the pressure band near C propagates counter-streamwise toward

The linear-time-invariance notion of the Koopman analysis

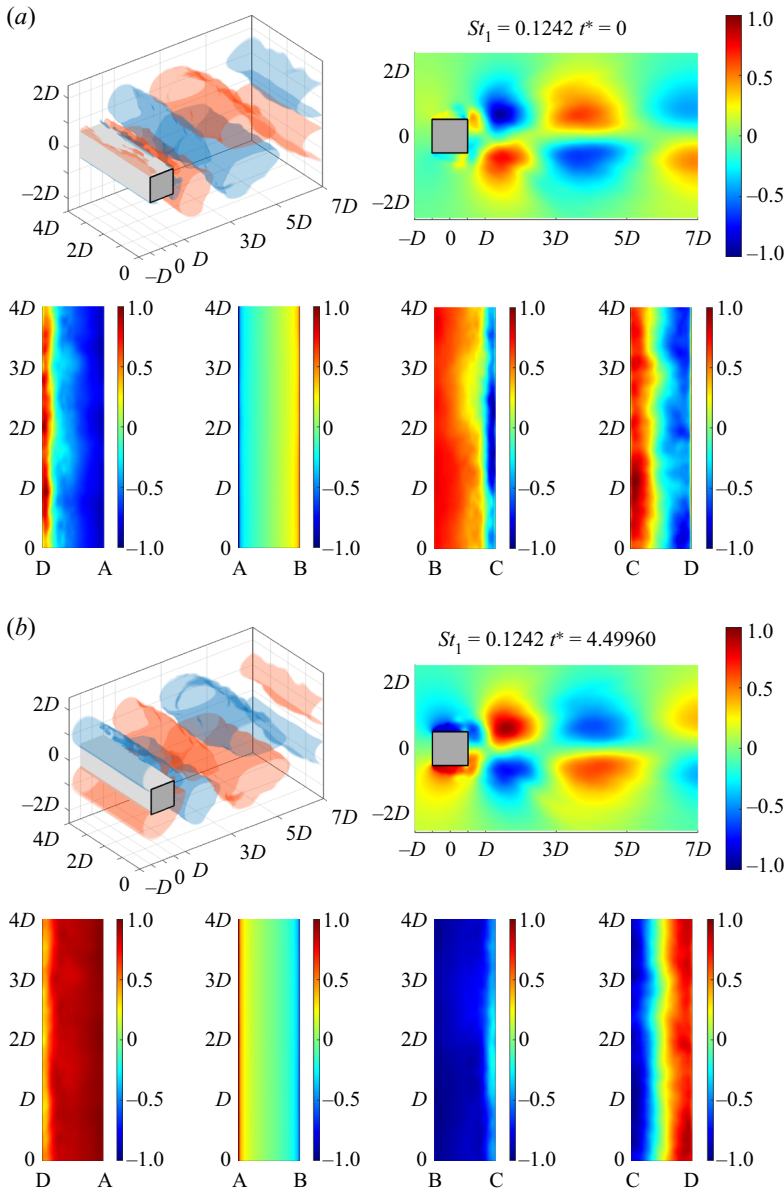


Figure 3. Normalized dynamic Koopman mode (-1 to 1) M_1 ($St_1 = 0.1242$) of P inside the flow domain and on the walls of the prism at (a) $t^* = 0$ and (b) $t^* = 4.49960$: iso-surfaces ± 0.25 of P (top left); mid-prism-span slice of P (top right); the bottom (DA), upstream (AB), top (BC) and downstream (CD) walls, respectively (bottom from left to right). Multimedia file slowed by a factor of 500.

B, through which negative pressure turns to positive in a sharp gradient across $1/5D$ (see figure 4a). The pressure band results from fluid reversing into the circulating zone, pushing against the forward-traveling mainstream. As the top shear layer disperses and gains curvature, its tendency to close the separation bubble bottlenecks the reverse flow, causing the band to decay in intensity. However, not until the exact moment of bubble closure does the shear layer curvature effectuate into actual reattachment (figure 4b). An immediate consequence is an intra-bubble pressure equalization. The low-pressure band

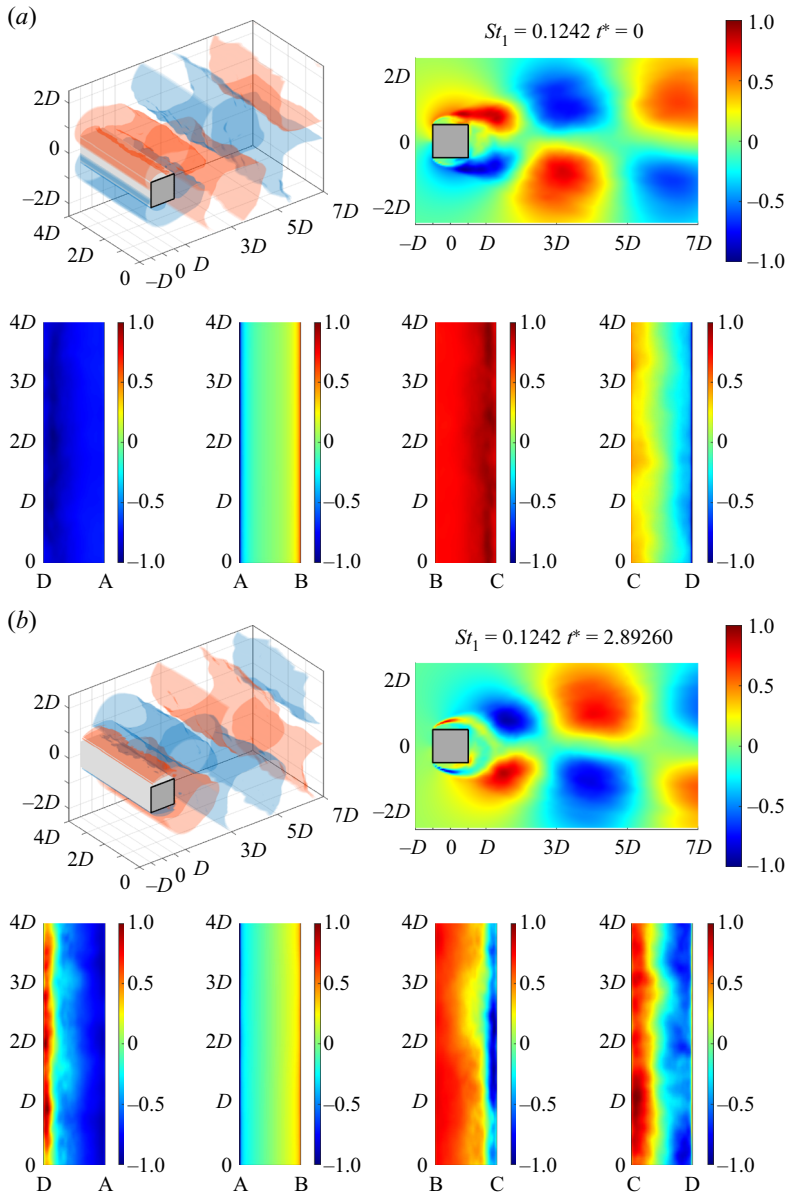


Figure 4. Normalized dynamic Koopman mode (-1 to 1) of M_1 ($St_1 = 0.1242$) of $|U|$ inside the flow domain and on the walls of the prism at (a) $t^* = 0$ and (b) $t^* = 2.89260$: iso-surfaces ± 0.25 of $|U|$ (top left); mid-prism-span slice of $|U|$ (top right); the bottom (DA), upstream (AB), top (BC) and downstream (CD) walls, respectively (bottom from left to right). Multimedia file slowed by a factor of 500.

also flips in sign as intense fluid carried by the shear layer impinges onto the wall upon reattachment.

The downstream wall (CD) also shows evidence of reattachment. A bisecting pressure band is observed, which separates the reaction pattern into two spanwise antisymmetric, opposite-sign halves. The two halves' intense pressures persist throughout the mode's periodicity and are only temporarily relieved as the wake structures cut off their turbulent sheets with the upstream (Sarpkaya 1979). Only at the exact moment of shedding, the two

halves rapidly switch signs and restore the pressure bi-polarity (see [figure 4b](#)). The pattern results from the curved shear layers approaching the downstream wall, as the sign of the two halves corresponds to that of the respective shear layer.

At this point, it is convenient to summarize the observations of M_1 into a lucid phenomenological process. An asymmetric wall jet resulting from forced, sharp-corner separation develops at the leading edge, shearing the fast external and slow internal fluid as a shear layer. The shear layer gains curvature and momentum thickness due to fluid dispersion and entrainment, both drawing it closer to the afterbody. The strong convection outside the shear layer also add to the curvature gain. The increasing curvature shortens the shear layer's lateral distance to the rear edge, bottlenecks the reverse flow and eventually culminates into reattachment. The reattachment, manifested as the closure of separation bubbles, suppresses the reverse flow altogether and stifles the shear layer's momentum transfer into the wake. Notwithstanding, the halt of momentum outlet is not accompanied by that of generation. As such, momentum continues to build up inside the enclosed bubble, dilating it in all directions. The dilation cannot penetrate the wall; it encounters a strong, incessant resistance from the oncoming free-stream, and an even stronger one from the leading edge jet. With no other option, the bubble's membrane-like structure succumbs to the continuous build-up at the feeblest point – the rear edge, unleashing the pent-up momentum and shedding fluid of coherent patterns into the prism base. This cyclic process was puzzled together after centuries of outstanding research (Nakamura & Nakashima 1986; Zhao *et al.* 2014; Trias, Gorobets & Oliva 2015; Portela, Papadakis & Vassilicos 2017; Bai & Alam 2018; Lander *et al.* 2018; Cao, Tamura & Kawai 2020; Chen *et al.* 2020, 2021, 2023; He *et al.* 2022), and is now effectively isolated and visualized by the Koopman-LTI.

Dissecting $|U|$ into individual velocity components exposes a consistent morphology in u and v , while w appeals to a different mechanism unrelated to the shear layers. Our investigation also supports the overwhelming contribution of u in the total content of $|U|$, as their dynamic behaviours display close resemblance (see [figure 10](#) from Part 1). The dynamic Koopman modes of M_1 of u , v and w are presented in the [Appendix figures 14–16](#) for concision.

3.1.3. *q-criterion*

A step forward is to examine vortex structures in the flow field. This paper presents q and Ω_R to exemplify the largely self-similar observations obtained from the second- and third-generation vortex criteria. We spare the first-generation because Gao & Liu (2018) and Jeong & Hussain (1995) made a critical distinction between vorticity and a vortex, deeming $|\omega|$ as obsolete. Accordingly, [figure 5](#) presents the normalized dynamic Koopman mode M_1 ($St_1 = 0.1242$) of q inside the flow domain and on the walls of the prism.

The most apparent coherent structures are identified alongside the shear layers. They are opposite-sign and outline the shear layers' momentum thickness, depicting two shearing interfaces between the jet stream and the surrounding flow. This is an elegant picture of the Kelvin–Helmholtz (KH) instability during shear layer transition II (Lander *et al.* 2016, 2018). We examine the top shear layer as an example. Fluid convects at low or even negative velocities inside the recirculation zone, so intense viscous shearing generates the inner interface as the forward-traveling jet encounters slow/reverse flow, causing the roll-up of the interfacial KH vortices. By contrast, the outer interface results from the jet stream shearing with the corner accelerated, external flow. Expectedly, [figure 5](#) shows that the outer and inner KH vortices have opposite-sign, appropriately describing the relative relationship between the two shearing interfaces. Afterwards, the KH structures convect

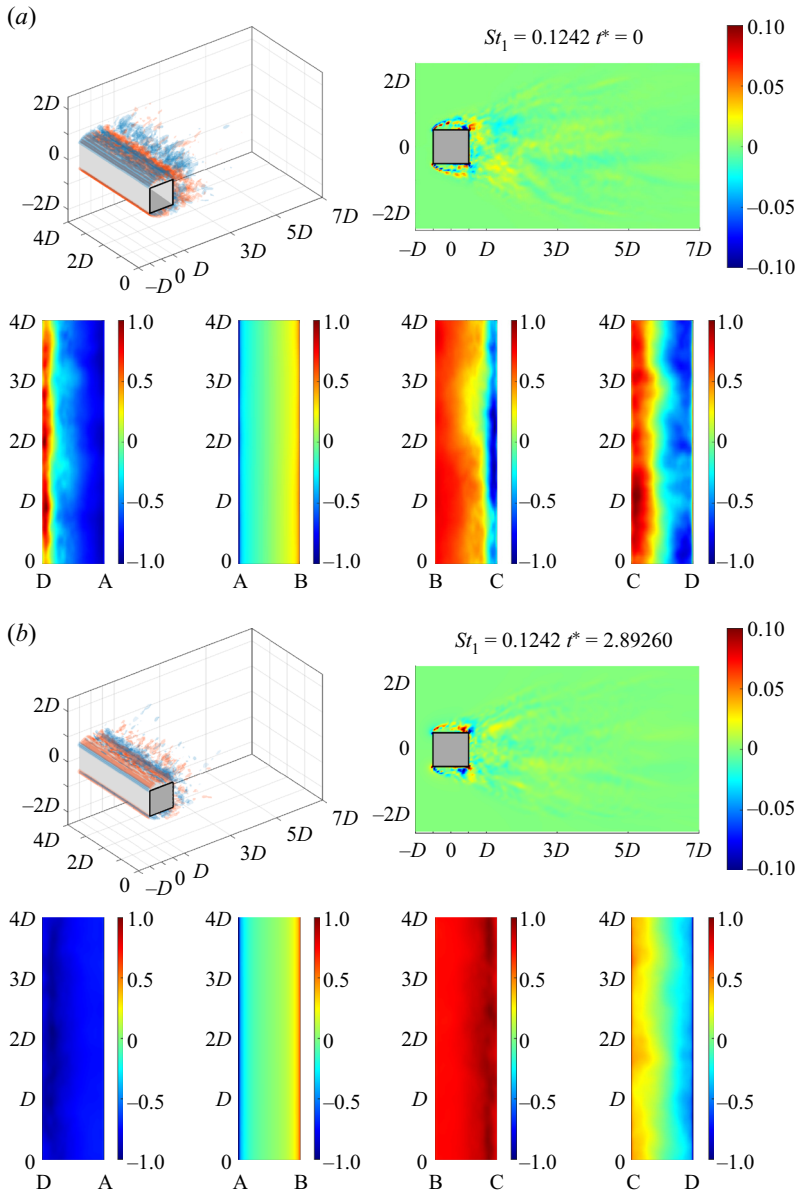


Figure 5. Normalized dynamic Koopman mode (-1 to 1) of M_1 ($St_1 = 0.1242$) of q inside the flow domain and on the walls of the prism at (a) $t^* = 0$ and (b) $t^* = 2.89260$: iso-surfaces ± 0.25 of q (top left); mid-prism-span slice of q (top right); the bottom (DA), upstream (AB), top (BC), and downstream (CD) walls, respectively (bottom from left to right). Multimedia file slowed by a factor of 500.

downstream alongside the curved shear layers. Figure 5(a) lucidly depicts how the rear corner cuts into a shear layer's inner interface, presenting unambiguous evidence of the leading vortex impingement and the destined collision of the KH vortices into the prism wall as the result of reattachment.

On a different note, though q appropriately depicts the KH instability, it fails to identify coherent vortex structures in the wake. The failure reflects the issue that Liu *et al.* (2019) discussed – the eigenvalue-based, second-generation criteria depend highly on

the user-defined threshold. Finding an appropriate one that suits both the global and local vortex scales is often difficult, if at all achievable. Threshold prescription is even trickier when the spatiotemporal content is transcribed into the Fourier space by the Koopman analysis. Therefore, though q , or the second-generation criteria in general, has rich information, controlling its threshold can be practically intractable after decomposing data into Koopman eigen tuples.

3.1.4. $\tilde{\Omega}_R$ -criterion

Avoiding the issue of threshold, [Figure 6](#) presents the normalized dynamic Koopman mode M_1 ($St_1 = 0.1242$) of the third-generation criterion $\tilde{\Omega}_R$ inside the flow domain and on the walls of the prism. An immediate observation is its resemblance with the velocity field, reaffirming the that the coherent structures observed in §§ 3.1.1 and 3.1.2 indeed result from vortical activities. However, there is an intriguing catch. A comparison of $|U|$ ([figure 3b](#)) and $\tilde{\Omega}_R$ ([figure 5b](#)) shows the shedding of the primary structures is escorted by an entourage of small-scale vortices. These smaller vortices are scattered in the near wake and do not necessarily conform to the borders of the primary structure. However, as the shedding progresses, the smaller vortices quickly dissipate, and only those within the primary structure survive ([figures 3a](#) and [6a](#)). A vortex's rotation acts as the shelter for small coherent structures.

On a methodical note, the downside of $\tilde{\Omega}_R$ is apparent too. The price of a universal threshold is the loss of local details. Though still vaguely visible, $\tilde{\Omega}_R$'s description of the shear layer's momentum thickness is less favourable, let alone the more intricate details of the interfacial KH vortices. To this end, the ratio-based criteria are not, at least for the scopes herein, necessarily an improvement of the eigenvalue-based criteria. It simply lends an alternative lens to examine vortex dynamics.

3.1.5. Broadband content

It shall be noted that the same exhaustive analysis has been conducted for every dynamic Koopman mode, but, for concision, only the most relevant discussions are presented in the subsequence. The less pivotal figures are assorted in the [Appendix](#).

The preceding discussions motivated an examination of the broadband content of the primary mode M_1 . The dynamic Koopman modes of M_2 ($St_2 = 0.1180$) and M_4 ($St_4 = 0.1304$) of $|U|$ inside the flow domain and on the walls of the prism are presented in the [Appendix figures 17](#) and [18](#). Analysis corroborates that M_2 and M_4 , though less energy-potent, are morphologically identical to M_1 , confirming their shared, broadband origin. The observation also extends to several other modes of adjacent frequencies, namely M_8 ($St_8 = 0.1428$), M_{10} ($St_{10} = 0.1118$), M_{11} ($St_{11} = 0.1366$), M_{12} ($St_{12} = 0.1056$) and M_{14} ($St_{14} = 0.1553$). The similitude confirms the conclusion drawn from Part 1, suggesting the broadband content of the primary peak is distributed across several frequency bins within $St = 0.1-0.15$ (see [figure 14\(a\)](#) from Part 1).

3.1.6. Longitudinal rolls

M_1 and its subsidiaries are related to shear layer dynamics, which result in the Bérnard–Kármán vortex shedding's primary structure – the rolls ([Hussain 1986](#)). Originating from forced separation, foreshadowed by fluid dispersion and shear layer curvature, instigated by reattachment and shear layers roll-up ([Wu et al. 1996](#)), and supplemented by the intra-shear layer Kelvin–Helmholtz instability ([Bloor 1964](#); [Gerrard](#)

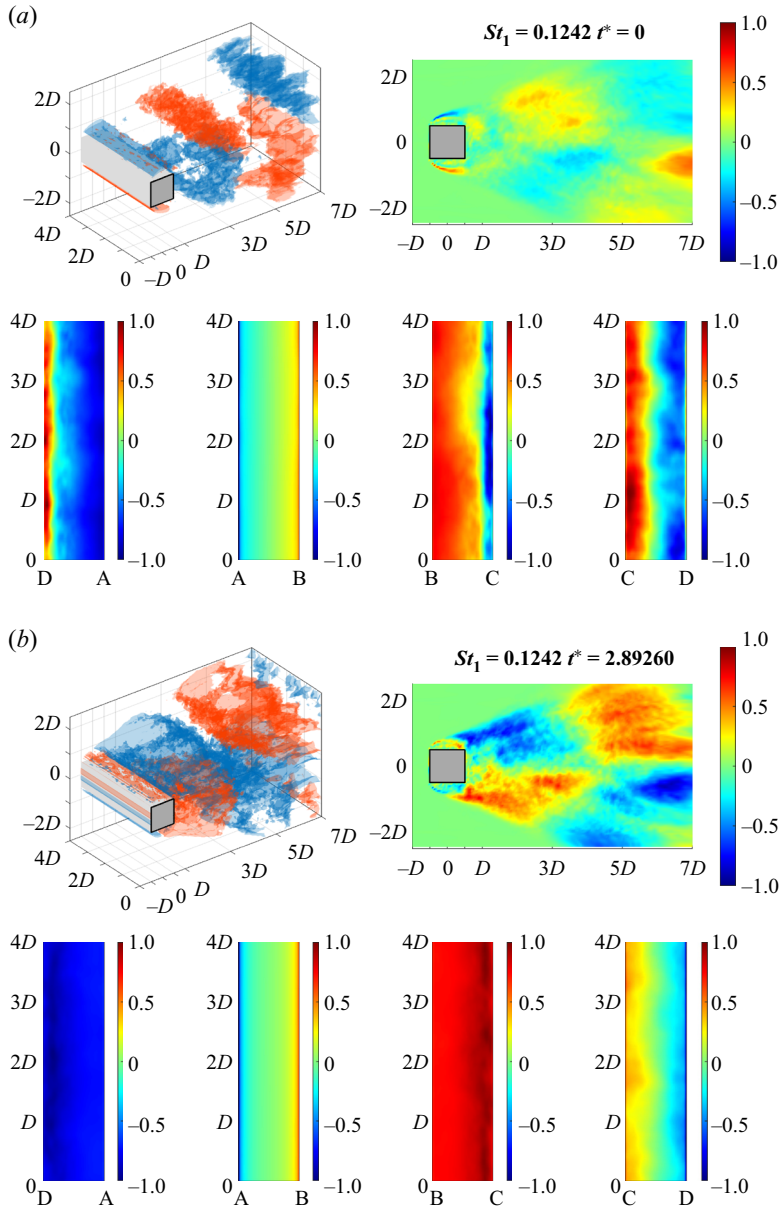


Figure 6. Normalized dynamic Koopman mode (-1 to 1) of M_1 ($St_1 = 0.1242$) of $\tilde{\Omega}_R$ inside the flow domain and on the walls of the prism at (a) $t^* = 0$ and (b) $t^* = 2.89260$: iso-surfaces ± 0.25 of $\tilde{\Omega}_R$ (top left); mid-prism-span slice of $\tilde{\Omega}_R$ (top right); the bottom (DA), upstream (AB), top (BC) and downstream (CD) walls, respectively (bottom from left to right). Multimedia file slowed by a factor of 500.

1966; Khor, Sheridan & Hourigan 2011), vorticity-infused fluid culminates into the span-wise longitudinal rolls, otherwise known as the Strouhal vortex (Wu *et al.* 1996).

The Koopman-LTI analysis isolated and pinpointed the structure's reattachment-type reactions due to the rolls. For engineering practice, the reduction of unsteady crosswind lift effectively comes down to the diminution of separation and reattachment. For example, chamfering the leading corners reduces the wall jets' intensity (Kwok, Wilhelm & Wilkie

1988), shortening the afterbody length prevents reattachment (Ongoren & Rockwell 1988; Luo *et al.* 1994; Zhao *et al.* 2014) and freestream turbulence weakens separation and so the correlations of forces (Vickery 1966; Lee 1975; McLean & Gartshore 1992; Lyn & Rodi 1994). Fascinatingly, based on the preceding analysis, one may infer that chamfering a prism's leading or trailing corners have fundamentally different effects.

3.2. M_5 – turbulence production

3.2.1. Tail-blob substructures

After M_1 , this section analyses the secondary mode of Class 1, M_5 . Figure 7 presents the normalized dynamic Koopman mode M_5 ($St_5 = 0.0497$) of P inside the flow domain and on the walls of the prism. The morphology notably differs from that of M_1 , in which two main types of wake substructures are observed (also shown by $\hat{\Omega}_R$ in the Appendix figure 19). The first, referred to as the tails, depicts the longitudinal, tail-like coherent structures that appear anti-symmetrically about the wake centreline. The tails cover the entire streamwise distance of the near-wake (figure 7a). The second, referred to as the blob, depicts a blob of fluid that adheres to the downstream wall (figure 7b). Interestingly, the tails and blob are separated by an opposite-sign cavity. Structure-wise, reattachment-type reactions are still observed on the crosswind walls. Nonetheless, the downstream wall, instead of the symmetric pattern of M_1 , reflects the overwhelming effect of the blob substructure: the negative pressure at mid-span depends directly on the size and intensity of the wall-adhering fluid.

Apart from P , the normalized dynamic Koopman mode M_5 of $|U|$, especially figure 8(b), unveils a note-worthy observation – M_5 originates from the shear layers, implying that M_1 and M_5 share origin and are interrelated. After a comprehensive analysis, it is concluded that M_5 describes the mechanisms of turbulence production. The tails are characteristic of the time-averaged production that includes the shear production with sufficient convection. In most turbulent free-shear flows, the mean velocity gradient and the mean momentum transfer are like-sign, resulting in a positive production and generation of the tail structures. This was originally observed by Hussain (1986) on turbulent jets (figure 9a).

3.2.2. Turbulence production in the prism wake

If one considers the prism wake as two stacked mixing layers or asymmetric wall jets, then the antisymmetric twin tail morphology comes as no surprise. However, the shear layers' non-symmetry brings about the issue of negative production, in which the zeros of the mean velocity gradient and the mean momentum transfer do not always coincide. The incongruence produces small regions where the mean velocity gradient and the mean momentum transfer are opposite-sign (figure 8a). The appearance of the cavity in figure 7(b) is precisely due to the negative production. The dynamic Koopman mode animates the cavity's gradual formation and intrusion into the originally one-piece structure, breaking it apart into the near-wake tail and wall-adhering blob substructures.

The source of turbulence production is vortex stretching and fluid entrainment. According to the serial work of Hussain, a substructure, known as ribs, arises from the stretching of the primary longitudinal rolls (Hussain & Zaman 1980; Hussain 1981, 1986; Hussain & Hasan 1985). While the shear layers continuously deposit vorticity into the rolls (the process illustrated by M_1), the ribs wrap around them in a helical fashion to enrich the longitudinal core's spanwise content. Vortex stretching drives the incessant entrainment of

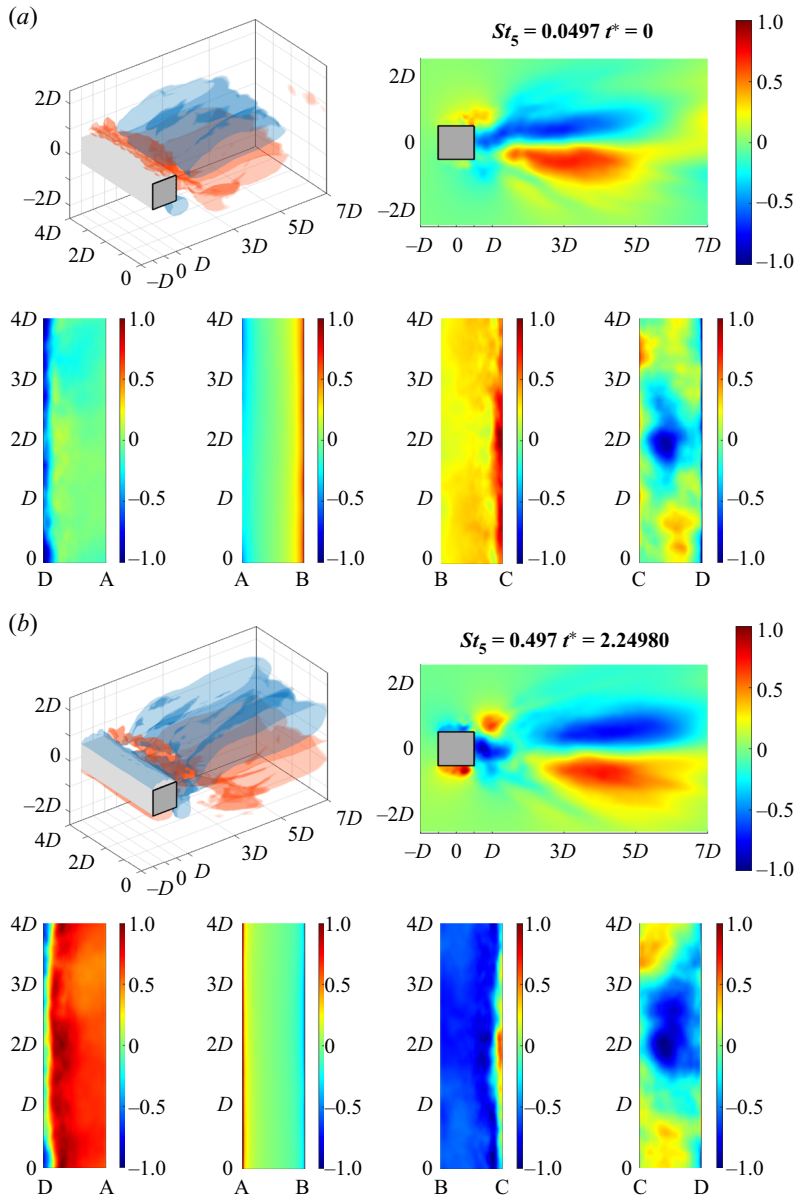


Figure 7. Normalized dynamic Koopman mode (-1 to 1) of M_5 ($St_5 = 0.0497$) of P inside the flow domain and on the walls of the prism at (a) $t^* = 0$ and (b) $t^* = 2.24980$: iso-surfaces ± 0.25 of P (top left); mid-prism-span slice of P (top right); the bottom (DA), upstream (AB), top (BC) and downstream (CD) walls, respectively (bottom from left to right). Multimedia file slowed by a factor of 500.

irrotational fluid into the vortex structures, and the location of fluid mixing is precisely at the rib-roll interface. This rib-roll entrainment process is like how a helically ribbed shaft rotates and draws meat into a meat grinder. As the shear layer curves towards the prism base, the negative production isolates the blob from the tail. Consequently, the rib-roll helix is imprinted onto the downstream wall, causing a staggered pattern in which the separatrix of the ribs separates the positive and negative regions (see figure 8b).

The linear-time-invariance notion of the Koopman analysis

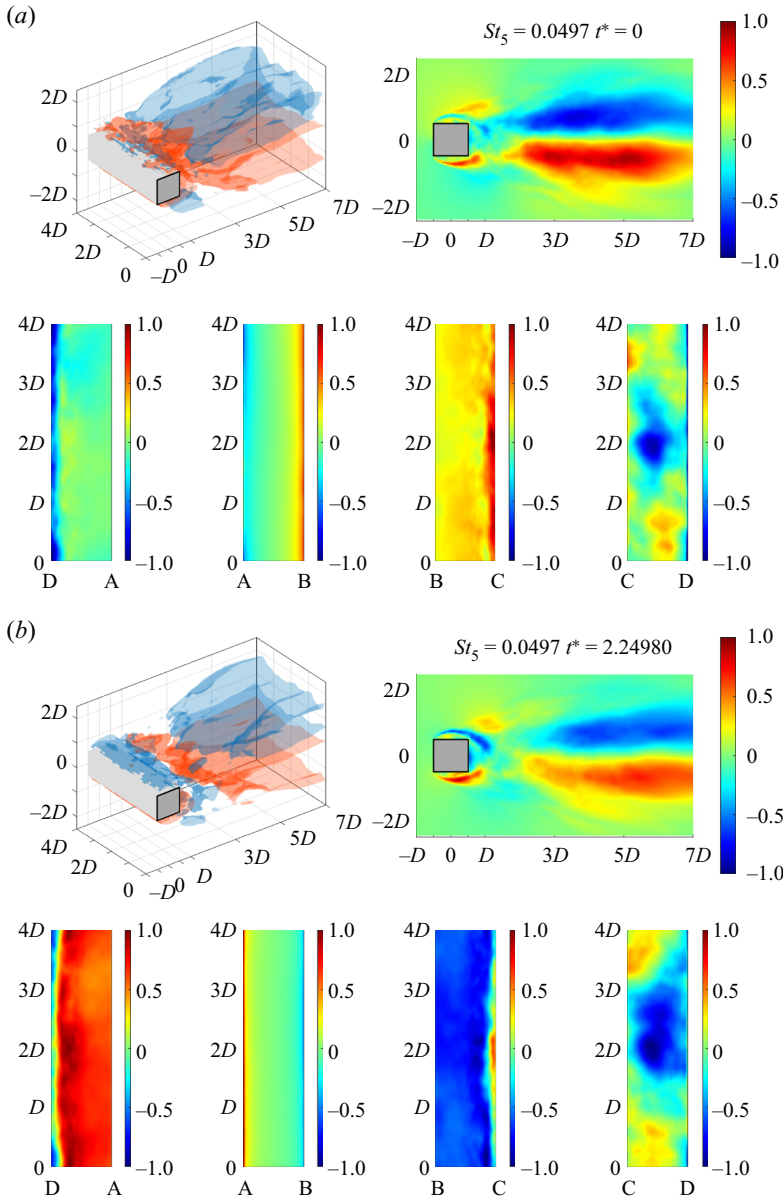


Figure 8. Normalized mode shapes (-1 to 1) of \mathcal{M}_5 ($St_5 = 0.0497$) of $|U|$ inside the flow domain and on the walls of the prism (a) $t^* = 0$ and (b) $t^* = 2.24980$: iso-surfaces ± 0.25 of $|U|$ (top left); mid-prism-span slice of $|U|$ (top right); the bottom (DA), upstream (AB), top (BC) and downstream (CD) walls, respectively (bottom from left to right). Multimedia file slowed by a factor of 500.

In sum, one may trace the shared origin of the Class 1 mechanisms, namely \mathcal{M}_1 and \mathcal{M}_5 , to the shear layer dynamics, the associated Bérnard–Kármán shedding and turbulence production. Class 1 corresponds to the most natural, energetic flow field structures that dominate the reactions of the on-wind wall. Their similarity in dynamical content also renders the three on-wind walls as a spectrally coupled fluid–structure interface, despite their geometric differences. However, the role of vortex stretching in turbulence production

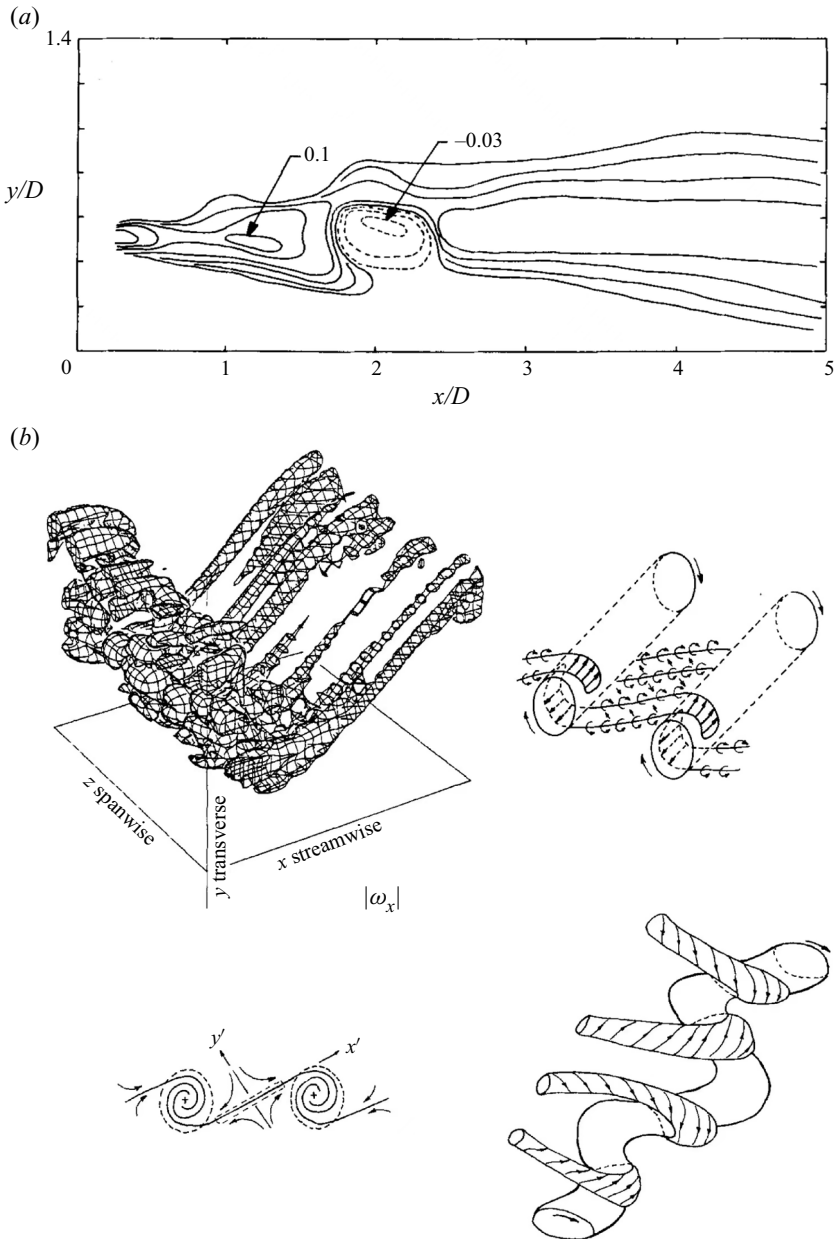


Figure 9. (a) Contour of time-averaged production and negative production (dotted) showing coherent structures in the near field of an axisymmetric jet at the instant of pairing in the jet column mode at $x \approx 1.75D$. Image taken from figure 3 of Hussain (1986). (b) Direct numerical simulation (top left) and a schematic illustration (top right) of rib-roll dynamics; flow details around a saddle (bottom left) and a more realistic picture of ribs and rolls. Image taken from figure 12 of Hussain (1986).

can be summarized as the consistent thinning (on statistical average) of fluid elements in the direction perpendicular to the stretching, reducing the radial length scale of the associated vortical structures and ultimately driving the downward cascade into the dissipative scales.

The linear-time-invariance notion of the Koopman analysis

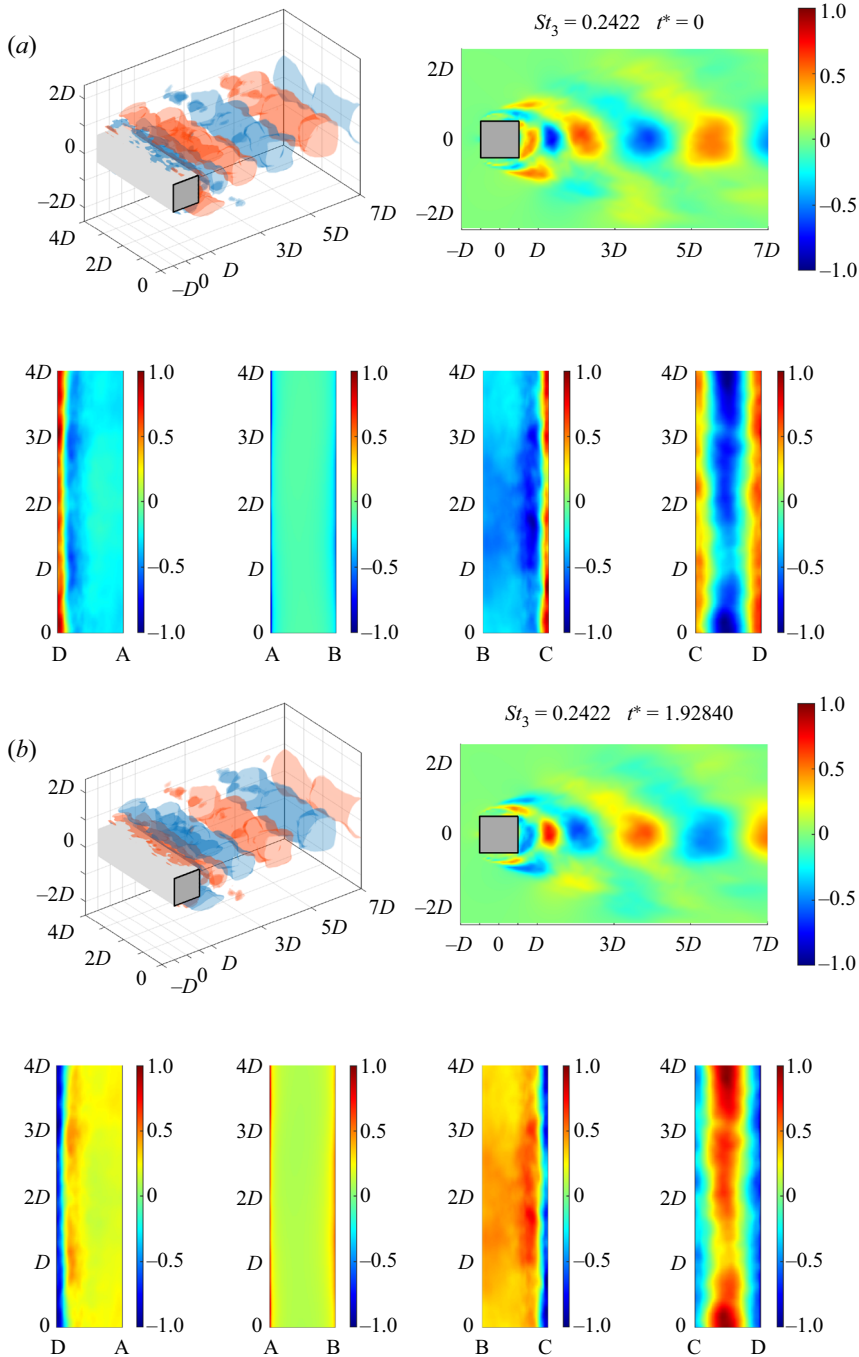


Figure 10. Normalized mode shapes (-1 to 1) of M_3 ($St_3 = 0.2422$) of $|U|$ inside the flow domain and on the walls of the prism at (a) $t^* = 0$ and (b) $t^* = 1.92840$: iso-surfaces ± 0.25 of $|U|$ (top left); mid-prism-span slice of $|U|$ (top right); the bottom (DA), upstream (AB), top (BC) and downstream (CD) walls, respectively (bottom from left to right). Multimedia file slowed by a factor of 500.

4. Phenomenological relationship (module 5) – Class 2

While the Class 1 mechanisms overwhelm the on-wind walls, their influence on the downstream wall is far from a monopoly. Part 1 identified four ancillary peaks at $St_3 = 0.2422$ (M_3), $St_7 = 0.0683$ (M_7), $St_9 = 0.1739$ (M_9) and $St_{13} = 0.1925$ (M_{13}), which overshadow the downstream wall. This section will analyse the phenomenology of the Class 2 mechanisms.

4.1. M_3 – second harmonic

To begin, [figure 10](#) presents the normalized dynamic Koopman mode M_3 ($St_3 = 0.2422$) of $|U|$ inside the flow domain and on the walls of the prism. The coherent structures are typical of the widely reported harmonic excitation (Ducoin, Loiseau & Robinet 2016; Kutz *et al.* 2016). It is also well known that the development of turbulence links closely to spatiotemporal wavefronts (Sengupta, Rao & Venkatasubbaiah 2006; Sengupta & Bhaumik 2011; Bhaumik & Sengupta 2014), so the detection of harmonics supports the investigation's correctness. The frequency $St_3 - 2St_1$ confirms M_3 is the second harmonic. Though spared from presentation, we also identified higher harmonics like the third harmonic M_{16} ($St_{16} = 0.3664$) $St_{16} - 3St_1$. M_3 plays a significant role in the spatiotemporal composition of the flow field (ranks the 4th in [table 1](#)) and the downstream wall (ranks the 9th), but its impacts on the on-wind walls are peripheral (ranks the 14th, 13th and 19th for BC, DA and AB, respectively). The observation substantiates a rudimentary principle – a dominant flow field mechanism does not necessarily incite strong reactions from the structure. Even after the global linearization optimally eliminated nonlinearities, the mechanisms of fluid–structure reactions/interactions are still perplexingly entwined.

As expected, the crosswind walls display the reattachment-type reactions, conforming to its harmonic lineage. The downstream wall displays a twin-band pattern instead of the mono-band structure of M_1 . For example, in [figure 10\(a\)](#), the negative pressure resides in the midspan, and the positive pressures appear near edges C and D. The opposite pressures are separated by two symmetric bands, doubling that of the fundamental mode in echo of the second harmonic. The structure reaction results from an axis-centric wake structure, which detaches the downstream wall starting from the midspan while its two legs linger on the rear edges. This arc oval shape induces a midspan suction with two positive-pressure zones near the edges (see [figure 10a](#)).

4.2. M_7 – subharmonic

Next, [figure 11](#) presents the normalized dynamic Koopman mode M_7 ($St_7 = 0.0683$) of $|U|$ inside the flow domain and on the walls of the prism. Aside from their frequency, M_7 and M_3 exhibit striking similarities. M_7 , too, originates from the shear layers. Its coherent structures are axis-centric about the wake centreline (particularly evident in P in the [Appendix figure 20](#)). Like M_3 , M_7 also has a considerable role in the flow field (ranks the 8th) and the downstream wall (ranks the 6th), but only triggers lukewarm reactions from the on-wind walls (ranks the 11th, 21st and 17th for BC, DA and AB, respectively). The indifference of the on-wind walls (or the susceptibility of the downstream wall) to Class 2 mechanisms is in sharp contrast with the Class 1 mechanisms, supporting the shared lineage of M_7 and M_3 . For its frequency $St_7 - 0.5St_1$, M_7 is the subharmonic of the primary structure M_1 . Our analysis also discovered that M_6 ($St_6 = 0.0745$) is the broadband twin of M_7 , whose mode shape is merely opposite-sign ([Appendix figures 21](#)

and 22). Ducoin *et al.* (2016) also made similar observations on the subharmonic peak in the wake of an SD7003 airfoil.

4.3. M_9 – ultra-harmonic

After pinpointing the second harmonic M_3 , third harmonic M_{16} and subharmonic M_7 , a natural next step is to search for the ultra-harmonic: M_9 is located with a frequency $St_9 = 1.5St_1$. Figure 12 presents the normalized dynamic Koopman mode M_9 ($St_7 = 0.1739$) of P inside the flow domain and on the walls of the prism, illustrating the axis-centric and sequential arrangement of the coherent structures (also $|U|$ in the Appendix figure 23). As anticipated, the downstream wall is again acutely sensitive to the excitation of the ultra-harmonic. M_9 , ranking only the 11th in the flow field dominance, generates the 2nd most impactful Class 2 reaction on the downstream wall.

Class 2 mechanisms root from harmonic excitation and are responsible for complicated patterns on the downstream wall. The similarity between M_3 , M_7 and M_9 unilaterally:

- (1) originate from the shear layers with a clear connection to the *Class 1* mechanisms (i.e. development of turbulence);
- (2) form inside the prism base ($< 2.5D$) where negative base pressure is incurred; and
- (3) remain axis-centric as coherent structures convect downstream.

4.4. M_{13} – 2P mode

At last, figure 13 presents the normalized dynamic Koopman mode M_{13} ($St_{13} = 0.1935$) of P inside the flow domain and on the walls of the prism. M_{13} resembles the other harmonics by dominating dynamics on the downstream wall, but fundamentally differs because its coherent structures are not axis-centric. Instead, two parallel, antisymmetric sequences form on either side of the wake axis. The reaction M_{13} instigated on the downstream wall is also different from its harmonic peers. The mono-band picture appeals to that of the primary structure M_1 (also $|U|$ in the Appendix figure 24).

To rationalize M_{13} , we look into its morphology. Three opposite-sign pairs are found in the wake between 0 and $5D$. In the same region, only two opposite-sign pairs are found for M_1 . Considering its frequency $St_{13} = 1.5St_1$, M_{13} is likely a second ultra-harmonic of the fundamental structure. However, unlike the axis-centric sequence of M_9 , the bi-sequential layout of M_{13} suggests its strong connection with the Kármán street.

M_{13} 's morphology alludes to the 2P mode originally observed in the wake of a vibrating cylinder after surpassing the initial branch (Williamson 1996; Williamson & Govardhan 2004). As described by Williamson & Roshko (1988), the 2P transition is incited when a cylinder's crosswind motion surpasses a critical value, generating a phase difference between two sub-vortices in a single shedding cycle. The phase difference prevents like-sign vortex amalgamation, and hence 2-Pairs (2P) of vortices instead of 2-Single (2S) ones form in the Kármán street. On this note, we must highlight the differences between the test subject in Williamson & Roshko (1988) and herein, which are aeroelastic versus stiff, and cylinder versus prism.

Nevertheless, is it possible that the 2P mode is a natural ultra-harmonic structure of the bluff body wake? One may rationalize how an oscillating cylinder generates phase differences in the Bérnard–Kármán vortex shedding: lacking sharp edges, a cylinder must rely on crosswind motions to prematurely break the turbulent sheet before vortex amalgamation. If the motions are not substantial enough, the wake remains in the preferred 2S state. However, in the reference frame of the cylinder, the only difference between a

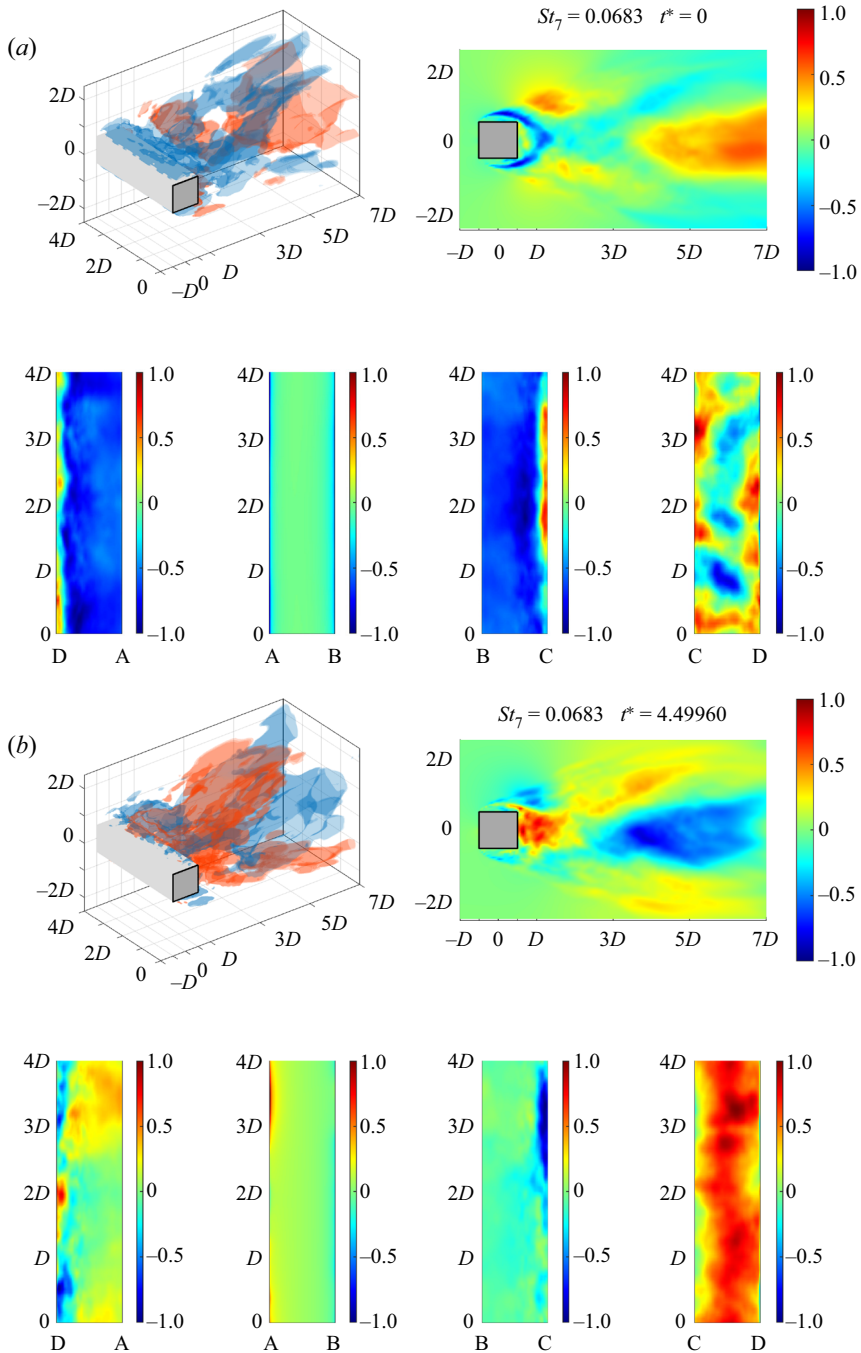


Figure 11. Normalized mode shapes (-1 to 1) of M_7 ($St_7 = 0.0683$) of $|U|$ inside the flow domain and on the walls of the prism at (a) $t^* = 0$ and (b) $t^* = 4.49960$: iso-surfaces ± 0.25 of $|U|$ (top left); mid-prism-span slice of $|U|$ (top right); the bottom (DA), upstream (AB), top (BC) and downstream (CD) walls, respectively (bottom from left to right). Multimedia file slowed by a factor of 500.

rigid and vibrating cylinder is the curvature of the shear layers, such that the greater the oscillation, the more curved the shear layers and the earlier the reattachment.

The linear-time-invariance notion of the Koopman analysis

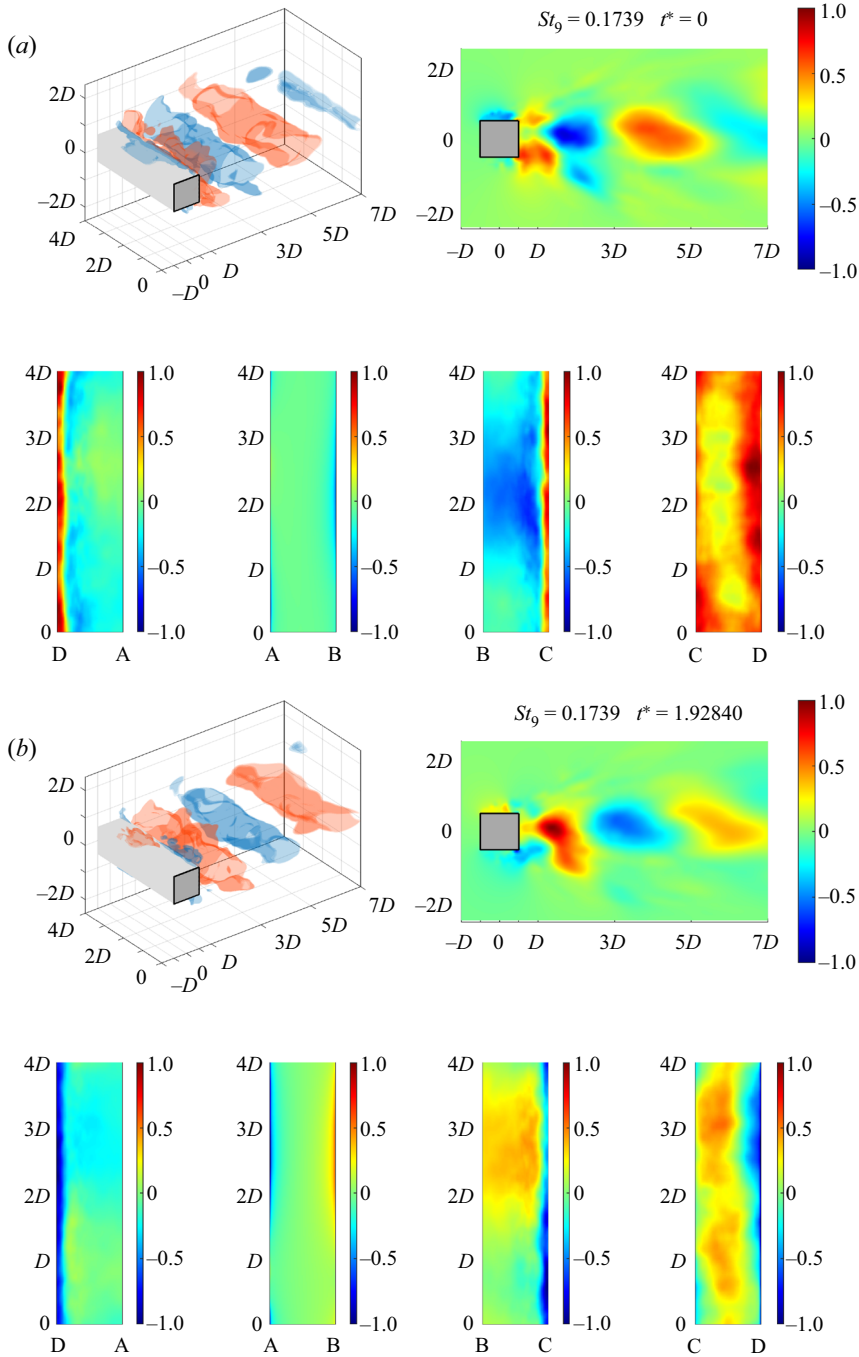


Figure 12. Normalized mode shapes (-1 to 1) of M_9 ($St_9 = 0.1739$) of P inside the flow domain and on the walls of the prism at (a) $t^* = 0$ and (b) $t^* = 1.92840$: iso-surfaces ± 0.25 of P (top left); mid-prism-span slice of P (top right); the bottom (DA), upstream (AB), top (BC) and downstream (CD) walls, respectively (bottom from left to right). Multimedia file slowed by a factor of 500.

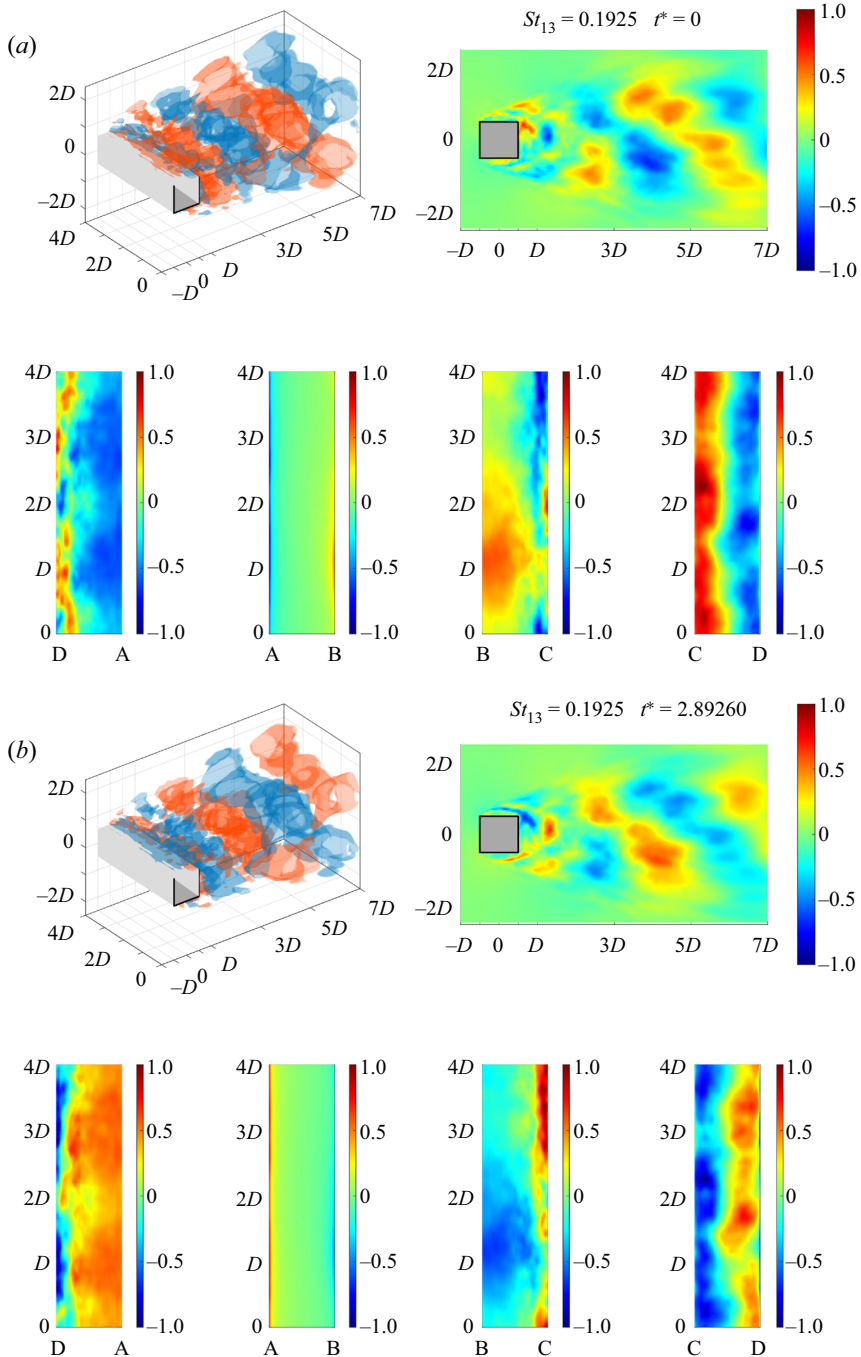


Figure 13. Normalized mode shapes (-1 to 1) of M_{13} ($St_{13} = 0.1925$) of P inside the flow domain and on the walls of the prism at (a) $t^* = 0$ and (b) $t^* = 2.89260$: iso-surfaces ± 0.25 of P (top left); mid-prism-span slice of P (top right); the bottom (DA), upstream (AB), top (BC) and downstream (CD) walls, respectively (bottom from left to right). Multimedia file slowed by a factor of 500.

What if other mechanisms can enhance the curvature for premature reattachment to the same effect? The shortening of the formation length with Re is widely known for the prism wake (Gerrard 1966; Williamson & Govardhan 2004), which is indeed due to increasingly curved shear layers. Compared to a curvilinear cylinder, a prism's sharp edges can incisively cut turbulent sheets when reattachment takes place. This means structure oscillation, as a way to encourage vortex shedding, is substitutable by sharp edges, nurturing a possibility for the premature shedding of phase-shifted vortices. If so, the 2P shedding in the rigid prism wake becomes spectrally embedded dynamics. Finally, the layouts of the other harmonics display a striking resemblance with that of the 2S mode (Williamson & Govardhan 2004; Morse & Williamson 2009) – axis-centric, alternating and vividly mono-sequential. Despite the phenomenological inferences, this topic demands further investigations.

5. New phenomenon: vortex breathing

At this point, the origins of the six dominant excitation-reaction mechanisms have been underpinned. The dynamic Koopman modes described the prism wake phenomenology with accuracy and insights. This paper also demonstrated the methodical procedure to arrive at the conclusions, which is replicable to other flows. One may also extend the conclusions to practical benefit: users can now target a specific fluid phenomenon to eliminate an undesired structural reaction. For example, one can use a splitter plate to prevent the axis-centric harmonic excitations, thus eliminating pressure extremities on the downstream wall and weaken turbulence development in the wake (Unal & Rockwell 1988*b*; Song *et al.* 2017).

In light of the preceding discussions, a new phenomenon was discovered. We detected an intriguing feature of the detached wake structures via dynamic visualization. Take the multimedia file of [figure 3](#) as an example, the coherent structures decay in intensity immediately after breaking their turbulent sheets with the separation bubbles. The decay, manifested as the contraction of the iso-surfaces and fading of colour between D and $3D$, is dissipation-wise natural and fully expected. However, surprisingly, these structures expand in size and grow in intensity between $3D$ and $5D$. This contraction-expansion motion repeats itself as if the vortices are inhaling and exhaling, and hence the vortex breathing.

The vortex breathing is fascinatingly perplexing because it disobeys intuitions. On a global scale, the total energy decays when all the modes are added together. Yet, for a single mode, if the initial intensity decay is related to the inter-molecular viscous dissipation, then what mechanisms account for the subsequent growth? After inspection, the breathing phenomenon is attributed to the energy exchange in and out of the discrete frequency bins. Given disparities in periodicity, the inhale of one Koopman mode corresponds to the exhale of some others. This exchange of modal energy is an accurate reflection of the wake's dynamic nature. A vortex's downstream convection incessantly injects vorticity into the irrotational fluid in its path, reeling them into circulation. It, too, constantly deposits viscously dissipated fluid in its trail. Therefore, there is a constant energy exchange in the circulation-entrainment-deposition process, which is captured by the energy in and out of a specific eigenfrequency. The onset, development and dissipation of turbulence also conform to spatiotemporal wavefronts, which certainly involve periodic/harmonic exchanges of energy. This also explains why sinusoids are excellent descriptors of the wake dynamics (see figure 8 in Part 1). The local, mode-wise vortex breathing phenomenon also calls for thoughts on its link to the energy cascade – the globally downward trend that permits inverse energy transfer (i.e. inverse cascade) on the local scale.

On a methodical note, vortex breathing demonstrates the importance of the dynamic Koopman mode. From figures 3(a) and 3(b) alone, the coherent structures between 3D and 5D appear, and quite naturally, less intense, less compact and more dispersed compared to their successors between D and 3D. The breathing motion would have been overlooked by a static Koopman mode. Conversely, a logical explanation would have been extremely difficult if the static snapshot was taken at the moment of exhaling, in which the downstream vortex appears more energetic. Dynamics of acute spatiotemporal sensitivity could have also been easily overlooked by static images due to the issue of phase.

6. Conclusions

This serial effort proposed a linear-time-invariance (LTI) notion, or the Koopman linearly time-invariant (Koopman-LTI) modular architecture, to associate fluid excitations and structure reactions. The LTI models reduced the pedagogical prism wake in the shear layer transition II to six dominant excitation-reaction mechanisms in Part 1. This Part 2 dynamically visualized the Koopman modes and unveiled new insights into the phenomenology of the prism wake. Specifically, two dynamic Koopman modes at $St_1 = 0.1242$ and $St_5 = 0.0497$ describe shear layer dynamics, Bérnard–Kármán shedding and turbulence production, which overwhelm the upstream and crosswind walls by the instigating reattachment-type of reactions. The dynamical similarity of the three walls also means they can be treated as a spectrally unified fluid–structure interface, despite their geometric disparity. Another four harmonic counterparts, namely the subharmonic at $St_7 = 0.0683$, the second harmonic at $St_3 = 0.2422$ and two distinct ultra-harmonics at $St_7 = 0.1739$ and $St_{13} = 0.1935$, dominate the downstream wall and only marginally affect the others. The 2P wake mode is also observed as an embedded harmonic of the bluff-body wake. This work also methodically proposed the dynamic Koopman mode, through which the vortex breathing phenomenon was discovered, which describes the constant and periodic energy exchanges in wake’s circulation-entrainment-deposition processes and turbulence development.

Supplementary movies. Supplementary movies are available at <https://doi.org/10.1017/jfm.2023.36>.

The original HD videos including those from the Appendix can be found at: <https://drive.google.com/drive/folders/1AHdhUdAfNwIC1XUUh-74PgQWW6jUHXJ5j?usp=?sharing>

Acknowledgements. We give a special thanks to the IT Office of the Department of Civil and Environmental Engineering at the Hong Kong University of Science and Technology. Its support for installing, testing and maintaining our high-performance servers is indispensable for the current project.



Funding. The work described in this paper was supported by the Research Grants Council of the Hong Kong Special Administrative Region, China (Project Nos. 16207719 and 16211821), the Fundamental Research Funds for the Central Universities of China (Project No. 2022CDJXY-016), the National Natural Science Foundation of China (Project Nos. 51908090, 42175180 and 74110-41030203), the Natural Science Foundation of Chongqing, China (Project No. 2022NSCQ-JQX2377), and the Key Project of Technological Innovation and Application Development in Chongqing (Project Nos. CSTB2022TIAD-KPX0145 and CSTB2022TIAD-KPX0142).

Declaration of interests. The authors report no conflict of interest.

Availability of data and material. The datasets generated during and/or analysed during the current work are restricted by provisions of the funding source but are available from the corresponding author on reasonable request.

Code availability. The custom code used during and/or analysed during the current work are restricted by provisions of the funding source.

Author ORCIDs.

-  Cruz Y. Li <https://orcid.org/0000-0002-9527-4674>;
-  Zengshun Chen <https://orcid.org/0000-0001-5916-1165>;
-  Tim K.T. Tse <https://orcid.org/0000-0002-9678-1037>;
-  Asiri Umenga Weerasuriya <https://orcid.org/0000-0001-8543-5449>;
-  Xuelin Zhang <https://orcid.org/0000-0003-3941-4596>;
-  Yunfei Fu <https://orcid.org/0000-0003-4225-081X>;
-  Xisheng Lin <https://orcid.org/0000-0002-1644-8796>.

Author contributions. C.Y.L and Z.C. contributed equally to this work. All authors contributed to the study conception and design. Funding, project management and supervision were led by T.K.T.T. and Z.C. and assisted by X.Z. Material preparation, data collection and formal analysis were led by C.Y.L. and Z.C., and assisted by A.U.W., Y.F. and X.L. The first draft of the manuscript was written by C.Y.L. and all authors commented on previous versions of the manuscript. All authors read, contributed and approved the final manuscript.

Compliance with ethical standards. All procedures performed in this work were in accordance with the ethical standards of the institutional and/or national research committee and with the 1964 Helsinki declaration and its later amendments or comparable ethical standards.

Consent to participate. Informed consent was obtained from all individual participants included in the study.

Consent for publication. Publication consent was obtained from all individual participants included in the study.

Appendix

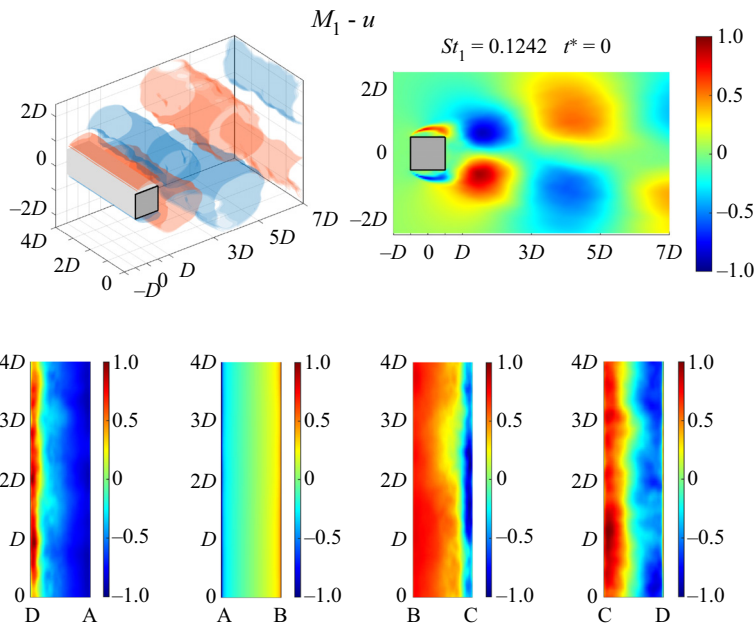


Figure 14. Normalized mode shapes (-1 to 1) of M_1 ($St_1 = 0.1242$) of u inside the flow domain and on the walls of the prism: iso-surfaces ± 0.25 of u (top left); mid-prism-span slice of u (top right); the bottom (DA), upstream (AB), top (BC) and downstream (CD) walls, respectively (bottom from left to right). Multimedia file slowed by a factor of 500.

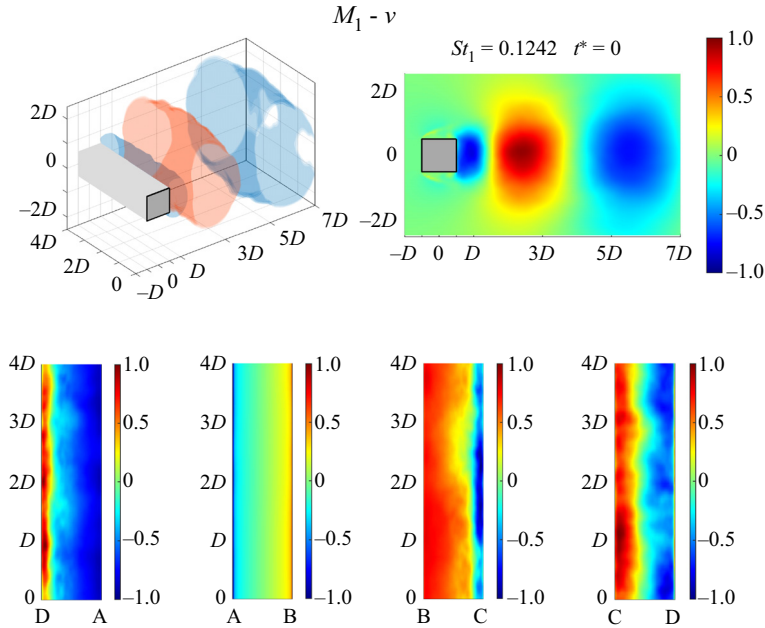


Figure 15. Normalized mode shapes (-1 to 1) of M_1 ($St_1 = 0.1242$) of v inside the flow domain and on the walls of the prism: iso-surfaces ± 0.25 of v (top left); mid-prism-span slice of v (top right); the bottom (DA), upstream (AB), top (BC), and downstream (CD) walls, respectively (bottom from left to right). Multimedia file slowed by a factor of 500.

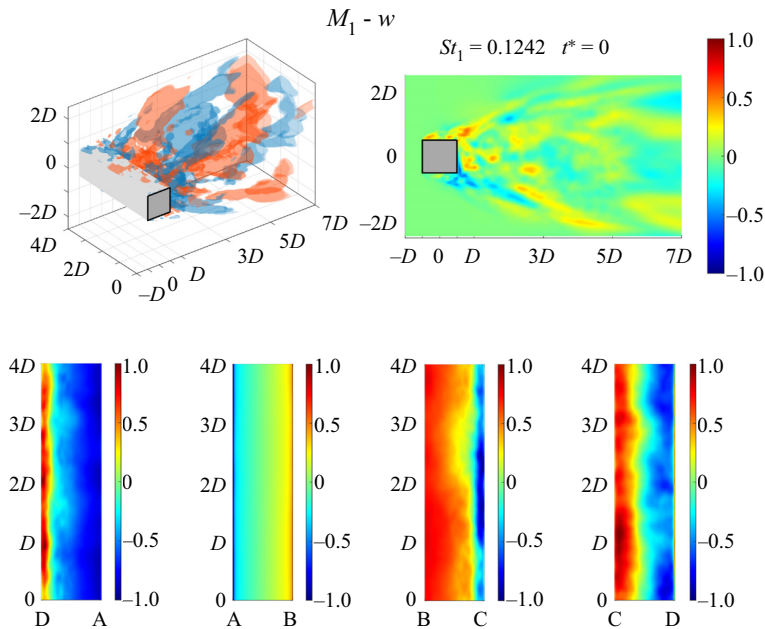


Figure 16. Normalized mode shapes (-1 to 1) of M_1 ($St_1 = 0.1242$) of w inside the flow domain and on the walls of the prism: iso-surfaces ± 0.25 of w (top left); mid-prism-span slice of w (top right); the bottom (DA), upstream (AB), top (BC) and downstream (CD) walls, respectively (bottom from left to right). Multimedia file slowed by a factor of 500.

The linear-time-invariance notion of the Koopman analysis

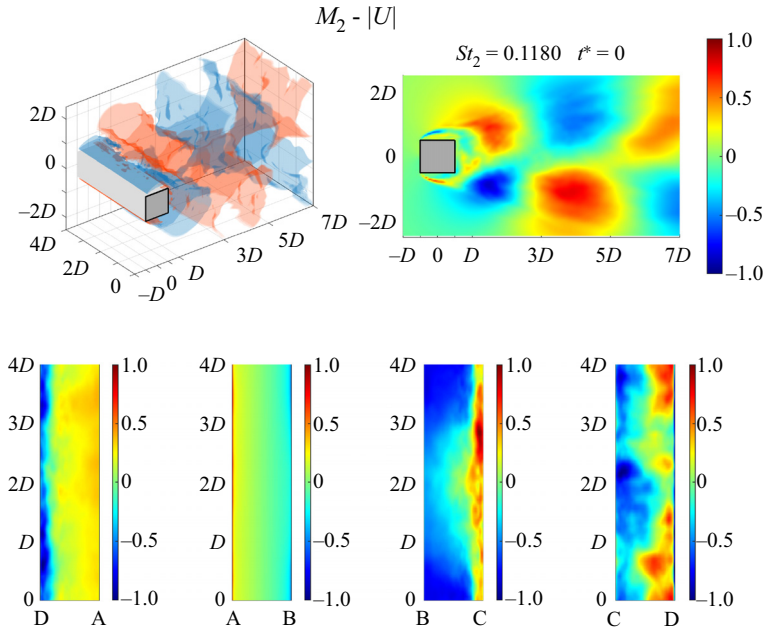


Figure 17. Normalized mode shapes (-1 to 1) of M_2 ($St_2 = 0.1180$) of $|U|$ inside the flow domain and on the walls of the prism: iso-surfaces ± 0.25 of $|U|$ (top left); mid-prism-span slice of $|U|$ (top right); the bottom (DA), upstream (AB), top (BC) and downstream (CD) walls, respectively (bottom from left to right). Multimedia file slowed by a factor of 500.

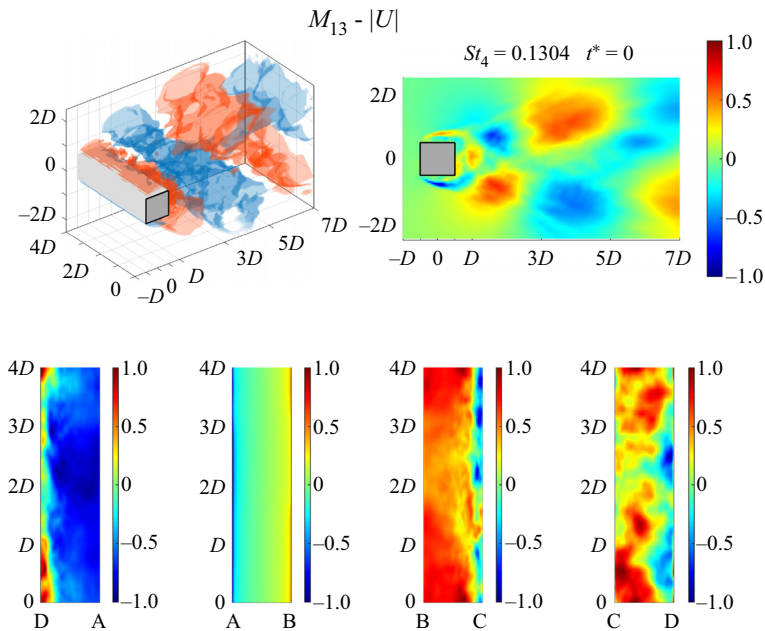


Figure 18. Normalized mode shapes (-1 to 1) of M_4 ($St_4 = 0.1304$) of $|U|$ inside the flow domain and on the walls of the prism: iso-surfaces ± 0.25 of $|U|$ (top left); mid-prism-span slice of $|U|$ (top right); the bottom (DA), upstream (AB), top (BC) and downstream (CD) walls, respectively (bottom from left to right). Multimedia file slowed by a factor of 500.

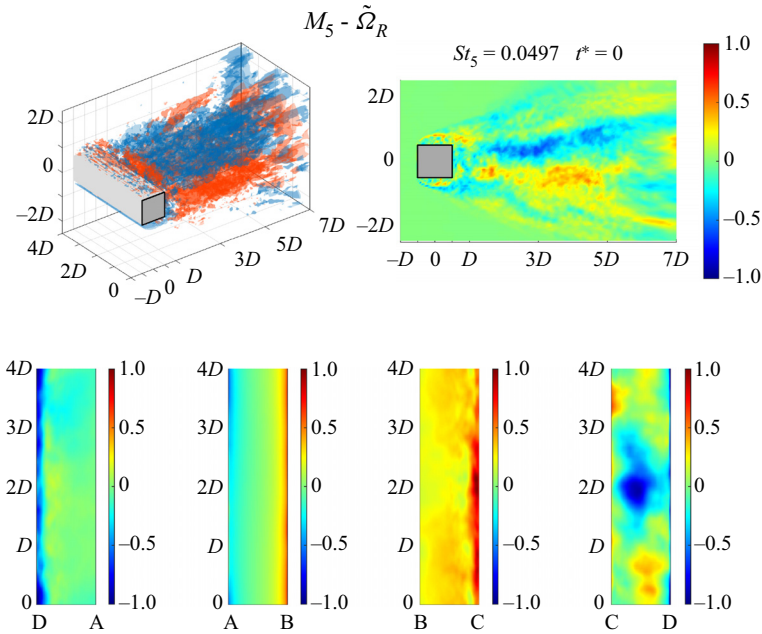


Figure 19. Normalized mode shapes (-1 to 1) of M_5 ($St_5 = 0.0497$) of $\tilde{\Omega}_R$ inside the flow domain and on the walls of the prism: iso-surfaces ± 0.25 of $\tilde{\Omega}_R$ (top left); mid-prism-span slice of $\tilde{\Omega}_R$ (top right); the bottom (DA), upstream (AB), top (BC) and downstream (CD) walls, respectively (bottom from left to right). Multimedia file slowed by a factor of 500.

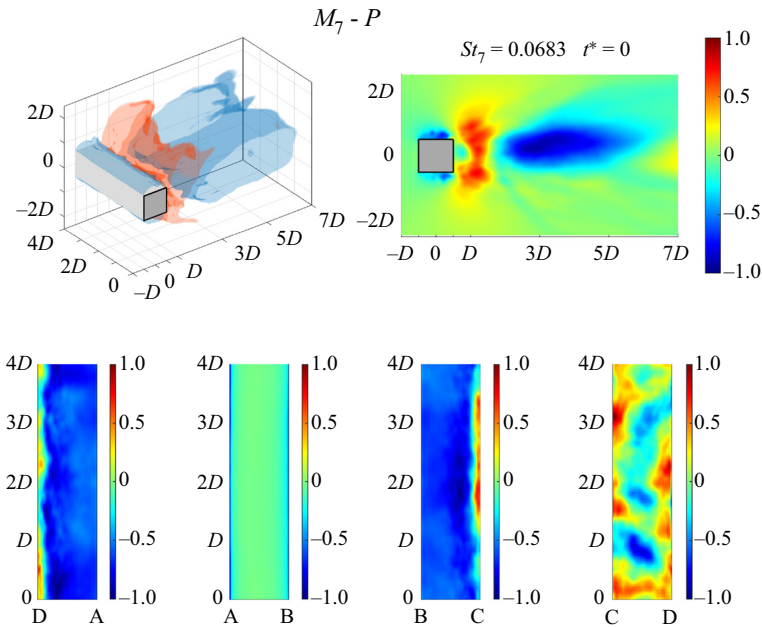


Figure 20. Normalized mode shapes (-1 to 1) of M_7 ($St_7 = 0.0683$) of P inside the flow domain and on the walls of the prism: iso-surfaces ± 0.25 of P (top left); mid-prism-span slice of P (top right); the bottom (DA), upstream (AB), top (BC) and downstream (CD) walls, respectively (bottom from left to right). Multimedia file slowed by a factor of 500.

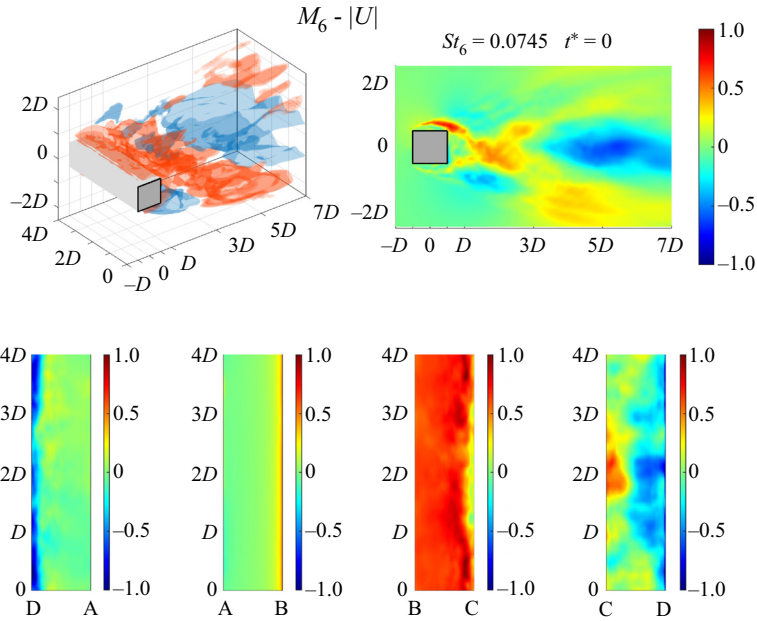


Figure 21. Normalized mode shapes (-1 to 1) of M_6 ($St_6 = 0.0745$) of $|U|$ inside the flow domain and on the walls of the prism: iso-surfaces ± 0.25 of $|U|$ (top left); mid-prism-span slice of $|U|$ (top right); the bottom (DA), upstream (AB), top (BC) and downstream (CD) walls, respectively (bottom from left to right). Multimedia file slowed by a factor of 500.

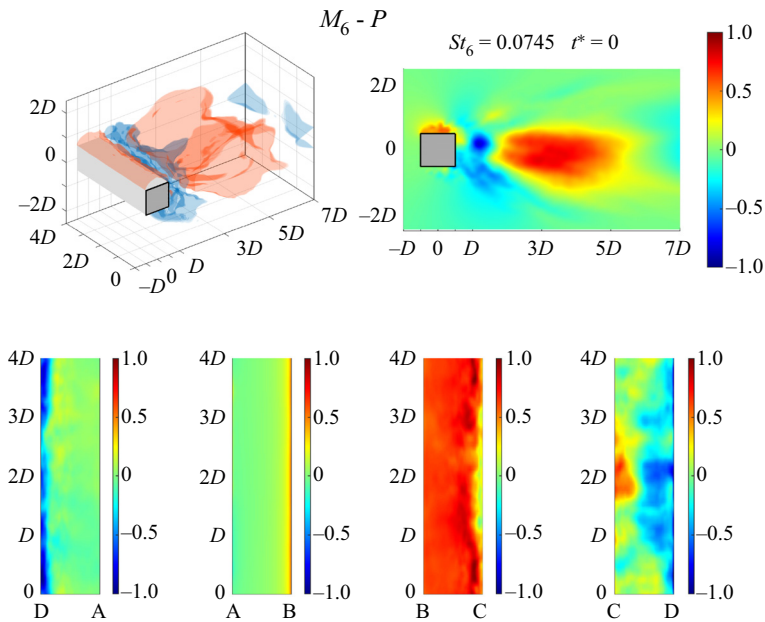


Figure 22. Normalized mode shapes (-1 to 1) of M_6 ($St_6 = 0.0745$) of P inside the flow domain and on the walls of the prism: iso-surfaces ± 0.25 of P (top left); mid-prism-span slice of P (top right); the bottom (DA), upstream (AB), top (BC) and downstream (CD) walls, respectively (bottom from left to right). Multimedia file slowed by a factor of 500.

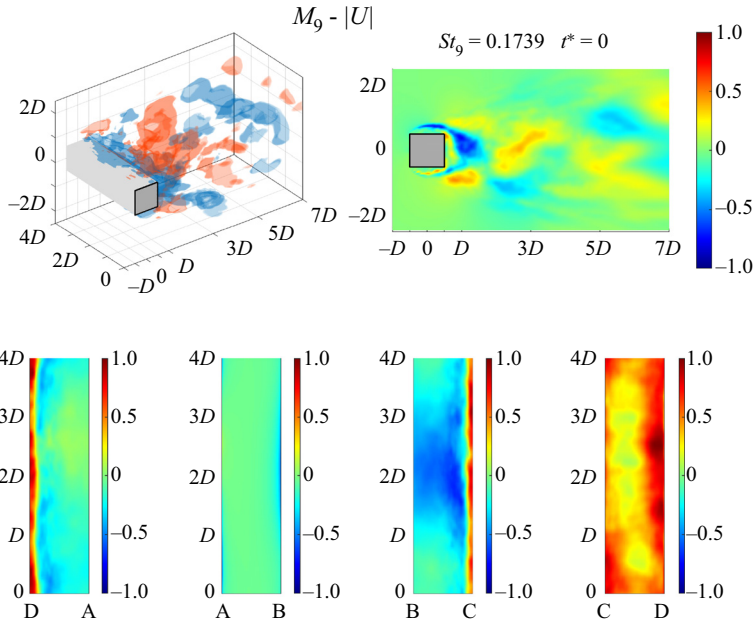


Figure 23. Normalized mode shapes (-1 to 1) of M_9 ($St_9 = 0.1739$) of $|U|$ inside the flow domain and on the walls of the prism: iso-surfaces ± 0.25 of $|U|$ (top left); mid-prism-span slice of $|U|$ (top right); the bottom (DA), upstream (AB), top (BC) and downstream (CD) walls, respectively (bottom from left to right). Multimedia file slowed by a factor of 500.

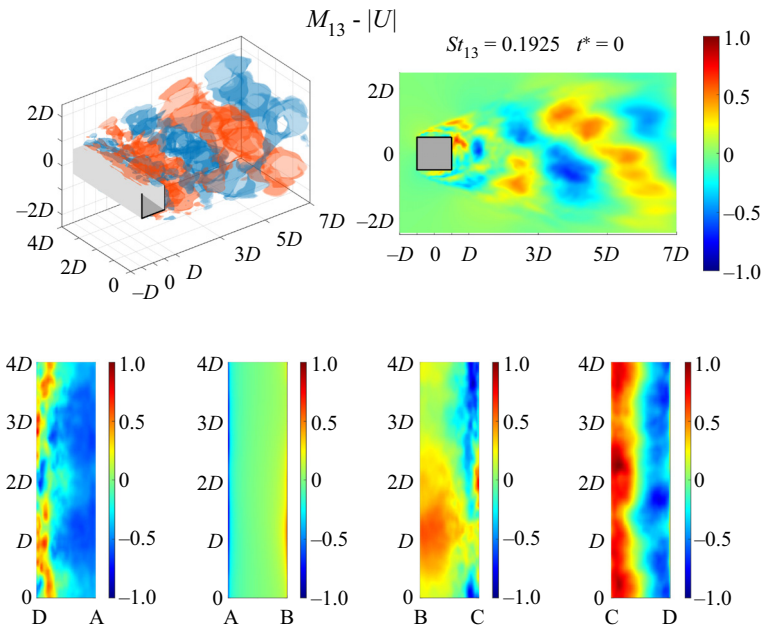


Figure 24. Normalized mode shapes (-1 to 1) of M_{13} ($St_{13} = 0.1925$) of $|U|$ inside the flow domain and on the walls of the prism: iso-surfaces ± 0.25 of $|U|$ (top left); mid-prism-span slice of $|U|$ (top right); the bottom (DA), upstream (AB), top (BC) and downstream (CD) walls, respectively (bottom from left to right). Multimedia file slowed by a factor of 500.

REFERENCES

- BAI, H. & ALAM, M.M. 2018 Dependence of square cylinder wake on Reynolds number. *Phys. Fluids* **30** (1), 015102.
- BHAUMIK, S. & SENGUPTA, T.K. 2014 Precursor of transition to turbulence: spatiotemporal wave front. *Phys. Rev. E – Stat. Nonlinear Soft Matt. Phys.* **89** (4), 043018.
- BLOOR, M.S. 1964 The transition to turbulence in the wake of a circular cylinder. *J. Fluid Mech.* **19** (2), 290–304.
- BRUNTON, S.L., PROCTOR, J.L., KUTZ, J.N. & BIALEK, W. 2016 Discovering governing equations from data by sparse identification of nonlinear dynamical systems. *Proc. Natl Acad. Sci. USA* **113** (15), 3932–3937.
- BUDIŠIĆ, M., MOHR, R. & MEZIĆ, I. 2012 Applied Koopmanism. *Chaos* **22** (4), 047510.
- CAO, Y., TAMURA, T. & KAWAI, H. 2020 Spanwise resolution requirements for the simulation of high-Reynolds-number flows past a square cylinder. *Comput. Fluids* **196**, 104320.
- CARLSSON, H., CARLSSON, C., FUCHS, L. & BAI, X.S. 2014 Large eddy simulation and extended dynamic mode decomposition of flow-flame interaction in a lean premixed low swirl stabilized flame. *Flow Turbul. Combust.* **93** (3), 505–519.
- CHEN, Z., FU, X., XU, Y., LI, C.Y., KIM, B. & TSE, K.T. 2021 A perspective on the aerodynamics and aeroelasticity of tapering: partial reattachment. *J. Wind Engng Ind. Aerodyn.* **212** (2020), 104590.
- CHEN, Z., HUANG, H., TSE, T.K.T., XU, Y. & LI, C.Y. 2020 Characteristics of unsteady aerodynamic forces on an aeroelastic prism: a comparative study. *J. Wind Engng Ind. Aerodyn.* **205**, 104325.
- CHEN, Z., WANG, Y., WANG, S., HUANG, H., TSE, K.T., LI, C.Y. & LIN, C. 2022 Decoupling bi-directional fluid–structure interactions by the Koopman theory: actualizing one-way subcases and the role of crosswind structure motion. *Phys. Fluids* **34** (9), 095103.
- CHEN, Z., ZHANG, L., LI, K., XUE, X., ZHANG, X., KIM, B. & LI, C.Y. 2023 Machine-learning prediction of aerodynamic damping for buildings and structures undergoing flow-induced vibrations. *J. Build. Engng* **63**, 105374.
- DOTTO, A., LENGANI, D., SIMONI, D. & TACCHELLA, A. 2021 Dynamic mode decomposition and Koopman spectral analysis of boundary layer separation-induced transition. *Phys. Fluids* **33** (10), 104104.
- DUCOIN, A., LOISEAU, J.-C. & ROBINET, J.-C. 2016 Numerical investigation of the interaction between laminar to turbulent transition and the wake of an airfoil. *Eur. J. Mech. (B/Fluids)* **57**, 231–248.
- EIVAZI, H., VEISI, H., NADERI, M.H. & ESFAHANI, V. 2020 Deep neural networks for nonlinear model order reduction of unsteady flows. *Phys. Fluids* **32** (10), 105104.
- GAO, Y. & LIU, C. 2018 Rortex and comparison with eigenvalue-based vortex identification criteria. *Phys. Fluids* **30** (8), 085107.
- GARICANO-MENA, J., LI, B., FERRER, E. & VALERO, E. 2019 A composite dynamic mode decomposition analysis of turbulent channel flows. *Phys. Fluids* **31** (11), 115102.
- GERRARD, J.H. 1966 The mechanics of the formation region of vortices behind bluff bodies. *J. Fluid Mech.* **25** (2), 401–413.
- HE, Y., ZHANG, L., CHEN, Z. & LI, C.Y. 2022 A framework of structural damage detection for civil structures using a combined multi-scale convolutional neural network and echo state network. *Engng Comput.* **1**, 1–19.
- HELMHOLTZ, H. 1858 Über Integrale der hydrodynamischen Gleichungen, welche den Wirbelbewegungen entsprechen. *J. Reine Angew. Math.* **55**, 25–55.
- HERRMANN, B., BADDOO, P.J., SEMAAN, R., BRUNTON, S.L. & MCKEON, B.J. 2021 Data-driven resolvent analysis. *J. Fluid Mech.* **918**, 10.
- HUNT, J.C.R., WRAY, A.A. & MOIN, P. 1988 Eddies, streams, and convergence zones in turbulent flows. In *Studying Turbulence Using Numerical Simulation Databases, Proceedings of the 1988 Summer Program*, pp. 193–208. NASA.
- HUSSAIN, A.K.M.F. 1981 *Coherent Structures and Studies of Perturbed and Unperturbed Jets* (ed. Federal Republic of Germany, Session 3-Experiments), Lecture, pp. 252–291. Springer-Verlag.
- HUSSAIN, A.K.M.F. 1986 Coherent structures and turbulence. *J. Fluid Mech.* **173**, 303–356.
- HUSSAIN, A.K.M.F. & HASAN, Z.M.A. 1985 Turbulence suppression in free turbulent shear flows under controlled excitation. Part 2. Jet-noise reduction. *J. Fluid Mech.* **150**, 159–168.
- HUSSAIN, A.K.M.F. & ZAMAN, K.B.M.Q. 1980 Vortex pairing in a circular jet under controlled excitation. Part 2. Coherent structure dynamics. *J. Fluid Mech.* **101** (3), 493–544.
- JANG, H.K., OZDEMIR, C.E., LIANG, J.H. & TYAGI, M. 2021 Oscillatory flow around a vertical wall-mounted cylinder: dynamic mode decomposition. *Phys. Fluids* **33** (2), 025113.
- JEONG, J. & HUSSAIN, A.K.M.F. 1995 On the identification of a vortex. *J. Fluid Mech.* **285**, 69–94.

- KHOR, M., SHERIDAN, J. & HOURIGAN, K. 2011 Power-spectral density estimate of the Bloor-Gerrard instability in flows around circular cylinders. *Exp. Fluids* **50** (3), 527–534.
- KIYA, M. & SASAKI, K. 1983 Structure of a turbulent separation bubble. *J. Fluid Mech.* **137**, 83–113.
- KOOPMAN, B.O. 1931 Hamiltonian systems and transformation in Hilbert space. *Proc. Natl Acad. Sci.* **17** (5), 315–318.
- KOOPMAN, B.O. & NEUMANN, J.V. 1932 Dynamical systems of continuous spectra. *Proc. Natl Acad. Sci.* **18** (3), 255–263.
- KUTZ, J.N., BRUNTON, S.L., BRUNTON, B.W. & PROCTOR, J.L. 2016 Dynamic mode decomposition: data-driven modeling of complex systems. In *Society for Industrial and Applied Mathematics*, vol. 32 (4). Society for Industrial and Applied Mathematics.
- KWOK, K.C.S., WILHELM, P.A. & WILKIE, B.G. 1988 Effect of edge configuration on wind-induced response of tall buildings. *Engng Struct.* **10** (2), 135–140.
- LANDER, D.C., LETCHFORD, C.W., AMITAY, M. & KOPP, G.A. 2016 Influence of the bluff body shear layers on the wake of a square prism in a turbulent flow. *Phys. Rev. Fluids* **1** (4), 44406.
- LANDER, D.C., MOORE, D.M., LETCHFORD, C.W. & AMITAY, M. 2018 Scaling of square-prism shear layers. *J. Fluid Mech.* **849**, 1096–1119.
- LEE, B.E. 1975 Some effects of turbulence scale on the mean forces on a bluff body. *J. Wind Engng Ind. Aerodyn.* **1**, 361–370.
- LI, C.Y., CHEN, Z., LIN, X., WEERASURIYA, A.U., ZHANG, X., FU, Y. & TSE, T.K.T. 2022a The linear-time-invariance notion to the Koopman analysis: the architecture, pedagogical rendering, and fluid–structure association. *Phys. Fluids* **34** (12), 125136.
- LI, C.Y., CHEN, Z. & TSE, T.K.T. 2022b Associating structure surface pressure with corresponding flow field excitation—the data-driven answer to fluid–structure interaction. In *8th European-African Conference on Wind Engineering (8EACWE) Proceedings* (ed. I. Calotescu, A. Chitez, C. Cosoiu & A.C. Vladut), pp. 103–106. Editura Conpress.
- LI, C.Y., CHEN, Z., TSE, T.K.T., WEERASURIYA, A.U., ZHANG, X., FU, Y. & LIN, X. 2021 Establishing direct phenomenological connections between fluid and structure by the Koopman-linearly time-invariant analysis. *Phys. Fluids* **33** (12), 121707.
- LI, C.Y., CHEN, Z., TSE, T.K.T., WEERASURIYA, A.U., ZHANG, X., FU, Y. & LIN, X. 2022c A parametric and feasibility study for data sampling of the dynamic mode decomposition: spectral insights and further explorations. *Phys. Fluids* **34** (3), 035102.
- LI, C.Y., CHEN, Z., TSE, T.K.T., WEERASURIYA, A.U., ZHANG, X., FU, Y. & LIN, X. 2022d A parametric and feasibility study for data sampling of the dynamic mode decomposition: range, resolution, and universal convergence states. *Nonlinear Dyn.* **107** (4), 3683–3707.
- LI, C.Y., CHEN, Z., TSE, T.K.T., WEERASURIYA, A.U., ZHANG, X., FU, Y. & LIN, X. 2022e Best practice for the dynamic mode decomposition in wind engineering applications. In *8th European-African Conference on Wind Engineering (8EACWE) Proceedings* (ed. I. Calotescu, A. Chitez, C. Cosoiu & A.C. Vladut), pp. 11–14. Editura Conpress.
- LI, C.Y., CHEN, Z., ZHANG, X., TSE, T.K.T. & LIN, C. 2023 Koopman analysis by the dynamic mode decomposition in wind engineering. *J. Wind Engng Ind. Aerodyn.* **232**, 105295.
- LI, C.Y., TSE, T.K.T. & HU, G. 2020a Reconstruction of flow field around a square prism using dynamic mode decomposition. In *The 4th Hong Kong Wind Engineering Society Workshop*, vol. 61. The Hong Kong Wind Engineering Society.
- LI, C.Y., TSE, T.K.T. & HU, G. 2020b Dynamic mode decomposition on pressure flow field analysis: flow field reconstruction, accuracy, and practical significance. *J. Wind Engng Ind. Aerodyn.* **205**, 104278.
- LIU, C. 2019 Rortex based velocity gradient tensor decomposition. *Phys. Fluids* **31** (1), 011704.
- LIU, C., GAO, Y.S., DONG, X.R., WANG, Y.Q., LIU, J.M., ZHANG, Y.N., CAI, X.S. & GUI, N. 2019 Third generation of vortex identification methods: Omega and Liutex/Rortex based systems. *J. Hydrodyn.* **31** (2), 205–223.
- LIU, C., GAO, Y., TIAN, S. & DONG, X. 2018 Rortex—a new vortex vector definition and vorticity tensor and vector decompositions. *Phys. Fluids* **30** (3), 035103.
- LIU, N.-H., LI, X.-R., HAO, P.-F., ZHANG, X.-W. & HE, F. 2021a Mode switch in tonal under-expanded impinging jets. *Phys. Fluids* **33** (12), 124102.
- LIU, Y., LONG, J., WU, Q., HUANG, B. & WANG, G. 2021b Data-driven modal decomposition of transient cavitating flow. *Phys. Fluids* **33** (11), 113316.
- LIU, Q., SUN, Y., YEH, C.A., UKEILEY, L.S., CATTAFESTA, L.N. & TAIRA, K. 2021c Unsteady control of supersonic turbulent cavity flow based on resolvent analysis. *J. Fluid Mech.* **925**, 5.
- LIU, C., WANG, Y., YANG, Y. & DUAN, Z. 2016 New omega vortex identification method. *Sci. China Phys. Mech. Astron.* **59** (8), 684711.

- LUO, S.C., YAZDANI, M., CHEW, G., & LEE, Y.T. & S, T. 1994 Effects of incidence and afterbody shape on flow past bluff cylinders. *J. Wind Engng Ind. Aerodyn.* **53** (3), 375–399.
- LUSCH, B., KUTZ, J.N. & BRUNTON, S.L. 2018 Deep learning for universal linear embeddings of nonlinear dynamics. *Nat. Commun.* **9** (1), 4950.
- LYN, D.A. & RODI, W. 1994 The flapping shear layer formed by flow separation from the forward corner of a square cylinder. *J. Fluid Mech.* **267**, 353–376.
- MAGIONESI, F., DUBBIOSO, G., MUSCARI, R. & DI MASCIO, A. 2018 Modal analysis of the wake past a marine propeller. *J. Fluid Mech.* **855**, 469–502.
- MAUROY, A. & MEZIĆ, I. 2012 On the use of Fourier averages to compute the global isochrons of (quasi)periodic dynamics. *Chaos* **22** (3), 033112.
- MCLEAN, I. & GARTSHORE, I. 1992 Spanwise correlations of pressure on a rigid square section cylinder. *J. Wind Engng Ind. Aerodyn.* **41** (1–3), 797–808.
- MEZIĆ, I. 2005 Spectral properties of dynamical systems, model reduction and decompositions. *Nonlinear Dyn.* **41** (1–3), 309–325.
- MEZIĆ, I. 2013 Analysis of fluid flows via spectral properties of the Koopman operator. *Annu. Rev. Fluid Mech.* **45** (1), 357–378.
- MIYANAWALA, T.P. & JAIMAN, R.K. 2019 Decomposition of wake dynamics in fluid–structure interaction via low-dimensional models. *J. Fluid Mech.* **867**, 723–764.
- MORSE, T.L. & WILLIAMSON, C.H.K. 2009 Flow forcing, wake modes, and transitions for a cylinder undergoing controlled oscillations. *J. Fluids Struct.* **25** (4), 697–712.
- MULD, T.W., EFRAIMSSON, G. & HENNINGSON, D.S. 2012 Flow structures around a high-speed train extracted using proper orthogonal decomposition and dynamic mode decomposition. *Comput. Fluids* **57**, 87–97.
- NAKAMURA, Y. & NAKASHIMA, M. 1986 Vortex excitation of prisms with elongated rectangular, H and [vdash] cross-sections. *J. Fluid Mech.* **163**, 149–169.
- ONGOREN, A. & ROCKWELL, D. 1988 Flow structure from an oscillating cylinder Part 1. Mechanisms of phase shift and recovery in the near wake. *J. Fluid Mech.* **191**, 197–223.
- PAGE, J. & KERSWELL, R.R. 2019 Koopman mode expansions between simple invariant solutions. *J. Fluid Mech.* **879**, 1–27.
- PORTELA, A.F., PAPADAKIS, G. & VASSILICOS, J.C. 2017 The turbulence cascade in the near wake of a square prism. *J. Fluid Mech.* **825**, 315–352.
- RAISSI, M., WANG, Z., TRIANTAFYLLOU, M.S. & KARNIADAKIS, G.E. 2019 Deep learning of vortex-induced vibrations. *J. Fluid Mech.* **861**, 119–137.
- ROSHKO, A. 1993 Perspectives on bluff body aerodynamics. *J. Wind Engng Ind. Aerodyn.* **49** (1–3), 79–100.
- ROWLEY, C.W. & DAWSON, S.T.M.M. 2017 Model reduction for flow analysis and control. *Annu. Rev. Fluid Mech.* **49** (1), 387–417.
- ROWLEY, C.W., MEZIĆ, I., BAGHERI, S., SCHLATTER, P. & HENNINGSON, D.S. 2009 Spectral analysis of nonlinear flows. *J. Fluid Mech.* **641**, 115–127.
- SARPKAYA, T. 1979 Vortex-induced oscillations: a selective review. *J. Appl. Mech.* **46** (2), 241–258.
- SCHMID, P.J. 2010 Dynamic mode decomposition of numerical and experimental data. *J. Fluid Mech.* **656**, 5–28.
- SCHMID, P.J. 2022 Dynamic mode decomposition and its variants. *Annu. Rev. Fluid Mech.* **54** (1), 225–254.
- SCHMID, P.J., LI, L., JUNIPER, M.P., PUST, O., LI, L., JUNIPER, M.P. & PUST, O. 2011 Applications of the dynamic mode decomposition. *Theor. Comput. Fluid Dyn.* **25** (1–4), 249–259.
- SENGUPTA, T.K. & BHAUMIK, S. 2011 Onset of turbulence from the receptivity stage of fluid flows. *Phys. Rev. Lett.* **107** (15), 154501.
- SENGUPTA, T.K., RAO, A.K. & VENKATASUBBAIAH, K. 2006 Spatiotemporal growing wave fronts in spatially stable boundary layers. *Phys. Rev. Lett.* **96** (22), 224504.
- SONG, J., HU, G., TSE, K.T., LI, S.W. & KWOK, K.C.S. 2017 Performance of a circular cylinder piezoelectric wind energy harvester fitted with a splitter plate. *Appl. Phys. Lett.* **111** (22), 223903.
- TAIRA, K., BRUNTON, S.L., DAWSON, S.T.M., ROWLEY, C.W., COLONIUS, T., MCKEON, B.J., SCHMIDT, O.T., GORDEYEV, S., THEOFILIS, V. & UKEILEY, L.S. 2017 Modal analysis of fluid flows: an overview. *AIAA J.* **55** (12), 4013–4041.
- TRIAS, F.X., GOROBETS, A. & OLIVA, A. 2015 Turbulent flow around a square cylinder at Reynolds number 22,000: a DNS study. *Comput. Fluids* **123** (22), 87–98.
- UNAL, M.F. & ROCKWELL, D. 1988a On vortex formation from a cylinder. Part 1. The initial instability. *J. Fluid Mech.* **190**, 491–512.
- UNAL, M.F. & ROCKWELL, D. 1988b On vortex formation from a cylinder. Part 2. Control by splitter-plate interference. *J. Fluid Mech.* **190**, 513–529.

- VICKERY, B.J. 1966 Fluctuating lift and drag on a long cylinder of square cross-section in a smooth and in a turbulent stream. *J. Fluid Mech.* **25** (3), 481–494.
- WILLIAMSON, C.H.K. 1996 Vortex dynamics in the cylinder wake. *Annu. Rev. Fluid Mech.* **28** (1), 477–539.
- WILLIAMSON, C.H.K. & GOVARDHAN, R. 2004 Vortex-induced vibrations. *Annu. Rev. Fluid Mech.* **36** (1), 413–455.
- WILLIAMSON, C.H.K. & ROSHKO, A. 1988 Vortex formation in the wake of an oscillating cylinder. *J. Fluids Struct.* **2** (4), 355–381.
- WU, J., SHERIDAN, J., HOURIGAN, K. & SORIA, J. 1996 Shear layer vortices and longitudinal vortices in the near wake of a circular cylinder. *Exp. Therm. Fluid Sci.* **12** (2), 169–174.
- WU, W., MENEVEAU, C. & MITTAL, R. 2020 Spatio-temporal dynamics of turbulent separation bubbles. *J. Fluid Mech.* **883**.
- ZHAO, J., LEONTINI, J.S., LO JACONO, D. & SHERIDAN, J. 2014 Fluid-structure interaction of a square cylinder at different angles of attack. *J. Fluid Mech.* **747** (2), 688–721.